

Electron transport in CdTe/ZnO radial nanowire array solar cells

Master's Thesis

Oscar Hallbäck

6/17/2013



Contents

Abstract.....	3
Sammanfattning	3
Location.....	3
Acknowledgements	3
1. Introduction.....	4
1.1 Objective.....	4
1.2 Background	4
1.3 Principle of solar cells.....	4
1.3.1 Figures of merit	6
1.3.2 Equivalent circuit.....	9
1.4 Nanowire-based solar cells.....	12
1.4.1 Advantages.....	12
1.4.2 ZnO/CdTe core shell nanowires	12
2. Theory	14
2.1 The Poisson and continuity equations	14
2.2 Transport mechanisms	14
2.2.1 Drift/diffusion.....	14
2.2.2 Thermionic emission.....	16
2.2.3 Tunneling	19
2.3 Recombination.....	21
2.4 Temperature dependence	22
3. Method.....	25
3.1 Simulation.....	25
3.2 Measurements.....	27
4. Results and discussion.....	29
4.1 Simulation.....	29
4.2 Measurements.....	38
5. Conclusions.....	40
6. Bibliography.....	41
7. Appendix.....	42
8. List of abbreviations.....	42

Abstract

This project was conducted during the spring of 2013 at the IMEP-LAHC laboratory in Grenoble, as part of their research into the electrical and optical properties of ZnO/CdTe-based radial nanowire array solar cells. Simulations with different transport mechanisms and physical properties of the semiconductors were made and compared to experimentally acquired data. It was confirmed that the nanowire array setup is advantageous compared to a conventional planar structure, and it was also found that quantum mechanical tunneling of electrons through crystal defects or impurities in the core/shell interface could be the main dark current transport mechanism.

Sammanfattning

Detta arbete genomfördes under våren 2013 på IMEP-LAHC-laboratoriet i Grenoble, som ett led i deras forskning kring de elektriska och optiska egenskaperna hos solceller baserade på ett rutnät av radiella ZnO/CdTe-nanotrådar. Simuleringar med olika transportmekanismer och fysikaliska egenskaper hos halvledarna utfördes och jämfördes med experimentella data. Det bekräftades att strukturen med nanotrådar är fördelaktig jämfört med konventionella planära strukturer, och det var också funnet att kvantmekanisk tunnling genom kristalldefekter eller orenheter i gränssnittet mellan yttre och inre lagret kunde vara mörkerströmmens främsta transportmekanism.

Location

IMEP-LAHC (Institut de Microélectronique Electromagnétisme et Photonique-Laboratoire d'Hyperfréquences et de Caractérisation) is a multidisciplinary laboratory, part of a larger scientific complex called Minatec. The research center is situated in the French Alpine city of Grenoble, which is a major European site for semiconductor research, development and production.

Acknowledgements

I would like to thank my supervisors Anne Kaminski-Cachopo and Jérôme Michallon for their endless support and patient explanations to the ever arising issues and questions I encountered during the research. I would also like to express my gratitude to IMEP-LAHC for providing me with the opportunity to investigate the peculiar subject of nanowire-based solar cells.

1. Introduction

1.1 Objective

The aim of this project is to investigate the carrier transport properties in a solar cell based on an array of vertically aligned nanowires with a radial CdTe/ZnO heterojunction as charge separator. Simulations are performed with Sentaurus Device TCAD (Technology Computer Aided Design), and the results are compared with experimentally acquired data from a comparable planar device.

1.2 Background

In light of current renewable energy trends, solar energy holds a bright future due to its huge potential – the terrestrial influx of energy from our sun is so abundant that it has the theoretical capability of providing the present human consumption thousandfold.

One of the most promising ways to harvest this virtually unlimited source of energy is through the conversion into electricity by the photovoltaic effect. Every photon that is absorbed by a semiconductor has by some way delivered its energy. If deliverance is through the excitation of a bound electron, it will be free to move and contribute to a current flow.

Solar cells have the advantage of being practically maintenance-free, where we see commercial products having a lifetime of several decades. Since the energy source is free, the main necessities are land area, installation and material which are all one-time investments.

Environmentally, solar cell power plants can be considered to be one of the greenest alternatives to traditional fossil fuels, leaving zero carbon footprint with the exception of the production and installation phases.

To be able to really compete with the classical power plant systems, cost reduction in the production of solar cells is of importance and this could be achieved through low-cost processing methods, cheaper materials and lower material quantities.

High power conversion efficiency is also important, especially in extraterrestrial applications such as spacecrafts and satellites, and the so-called Shockley-Queisser [1] limit governs an upper boundary of the possible theoretical efficiency a single pn-junction solar cell can possess.

1.3 Principle of solar cells

A solar cell converts the energy from light into electrical energy, and relies on the photovoltaic principle. This principle explains that the energy of photons, which is defined by their wavelength, can be transferred to an electron that is bound to the crystal atoms in a semiconductor (an electron in the *valence band* (E_V)). If the energy of the photon is sufficient, the valence electron will be excited to the *conduction band* (E_C) of the semiconductor, where it is free to move. In between the valence- and conduction band, there is an energy gap where no *states* exist, called the *band gap* (E_G). This means that a photon only can be absorbed and excite an electron if its energy is larger than the band gap. Whenever an electron (which has a negative charge) is excited to the conduction band, it will leave an empty spot in the atom it originated from. This empty spot is called a *hole* and carries a positive charge (since the atom now lacks one electron). The net result is the *generation* of an *electron-hole pair*. The holes are also free to move by the exchange of valence electrons in neighboring atoms, and can be seen as imaginary *carriers* of positive charge. Whenever a hole and a

conduction electron meet each other, the electron will again be bound to the atom, lose its kinetic energy (through the emission of a photon, or lattice vibrations), and both charge carriers are annihilated. This is called *recombination*. Not only photons can generate electron-hole pairs. The crystal lattice vibrations (*temperature*) are also able to *thermally* excite an electron.

To be able to collect the energy caused by the creation of these opposing charges, they have to be separated. This is done by a *junction*, which is an area where the properties of the cell are intentionally modified so that the band structure is changing. The change in band structure (that is, the energy levels of the valence- and conduction bands are changed) is due to the creation of an electric field, which pulls the electrons in one direction and the holes in another (since they have opposing charges). The junction can consist of the interface between different semiconductors, a *heterojunction*, or the same semiconductor material, a *homojunction*. In the latter case, the change of energy band level is achieved through the change of *doping*. Doping is the intentional introduction of impurity atoms, which very easily leave an electron (n-doping), or a hole (p-doping) through thermal ionization. The fixed ions of opposing charge at either side of the junction will impose an electric field which separates the charge carriers.

Figure 1 pictures the band diagram for a pn-homojunction in a solar cell at room temperature, under four different scenarios. To the left in each diagram, we have the p-side, and to the right we have the n-side. The blue dots represent holes in the valence band (lower blue curve), and the red dots represent electrons in the conduction band (upper blue curve). The dashed line is the *Fermi level* which is the electrochemical potential for electrons. At the p-side, the single conduction electron is thermally excited, and the many holes are introduced through doping with *acceptor* atoms. Similarly, at the n-side, we have a single thermally generated hole and many electrons caused by ionization of *donor* atoms. When no bias is applied and the cell is not illuminated (A), the system is in *thermal equilibrium* in where the processes of generation, recombination and charge carrier movement from one side to another (*carrier injection*) is perfectly balanced so that the net result is zero. Now let's look at scenario B.

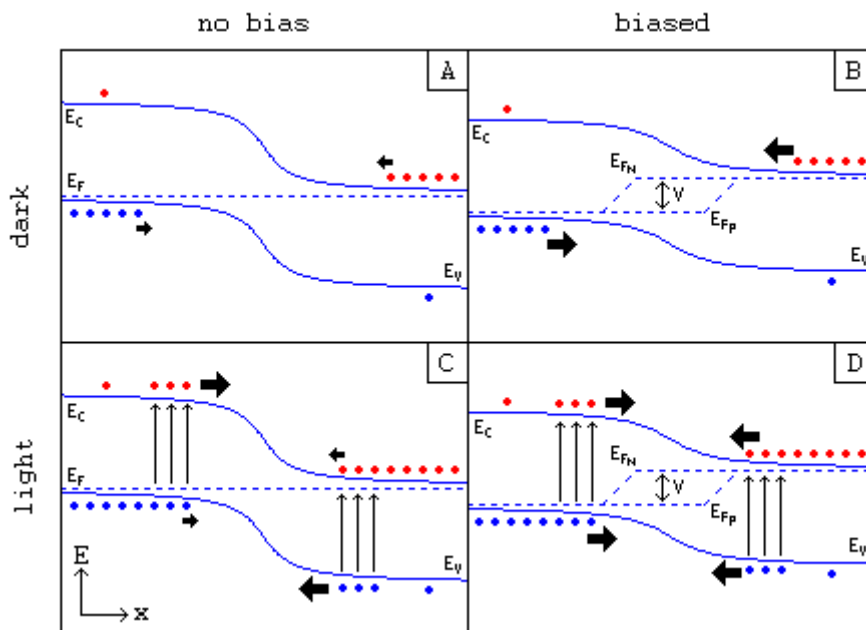


Figure 1: Band diagrams over a pn-junction during four different scenarios.

If we apply a voltage between the two sides, and supply the system with electrons through a current source, while still being in the dark, charge carriers starts to flow. The electric field caused by the junction is no longer sufficient to balance the amount of carriers approaching it diffusively. When dealing with solar cells, we call this *forward diode current* in the absence of illumination as the *dark current*. We are no longer under thermal equilibrium since excess carriers are introduced through the contacts. This leads to the necessity of defining separate Fermi levels for the electrons and holes, called *quasi-Fermi levels* (E_{Fn} and E_{Fp}). The difference between them in the junction is the applied bias, and reflects the change in electrochemical potential when moving from one side to another. Since the densities of electrons and holes increases exponentially (through the density-of-states function and the Fermi-Dirac function) the closer their quasi-Fermi level is to the conduction band and valence band edge respectively, the current of charge carriers being injected over the junction will increase exponentially with applied bias. In a perfect pn-junction, this current-voltage relation can be described by the *ideal diode law*.

If we switch off the bias for a moment, and instead turn on the light, we have a system that can be described by scenario C. Depending on the spectrum and intensity of the light that illuminates the solar cell, there will be a certain rate of *optically generated* charge carriers. At room temperature and under normal illumination conditions, this rate is much higher than the thermal generation rate. If an optically generated carrier manages to diffuse to the junction, it will quickly be swept over by the electric field to the other side. This creates a charge imbalance, and if there are good contacts connected, this imbalance is swiftly remedied by sending out a charge carrier to the circuit. The ratio between the charge carrier collection rate to the optical generation rate (for a given wavelength) is called the *internal quantum efficiency*. Similarly, there is a metric called the *external quantum efficiency*, which is the ratio between the charge carrier collection rate to the *incident* photon flux for a given wavelength. Minimizing recombination losses in all parts of the solar cell is essential for achieving high collection efficiency. The current from a solar cell under illumination and without any applied bias is called the *short-circuit current* I_{sc} , and it is the greatest current that is possible to extract.

In the previous scenario, a lot of charge carriers were generated and hopefully collected. But since there was no potential difference between the two sides, no power was extracted. If we apply a load to the cell (scenario D), for example a resistor, we can make use of the flow of charge carriers. This creates a potential drop which changes the band structure just as in B. As the potential drop increases with a greater load, more charge carriers starts to flow in the opposite direction, lowering the amount of current going through the load. When the size of the load causes a potential that makes the current through the load to be exactly zero, the cell is called to be in an open-circuit condition and the corresponding voltage is called the *open-circuit voltage* V_{oc} . Consequently, there is a certain voltage in between zero (where we have maximum current, but no voltage) and V_{oc} (where we have maximum voltage, but no current) yielding maximum power. This voltage, in conjunction with its corresponding current, is called the *maximum power point*.

1.3.1 Figures of merit

Every solar cell can be classified by a number of important parameters. These will tell us the characteristics and performance of its charge carrier generation and retrieval, and they are mainly deduced from the I-V curve measured under illumination (figure 2).

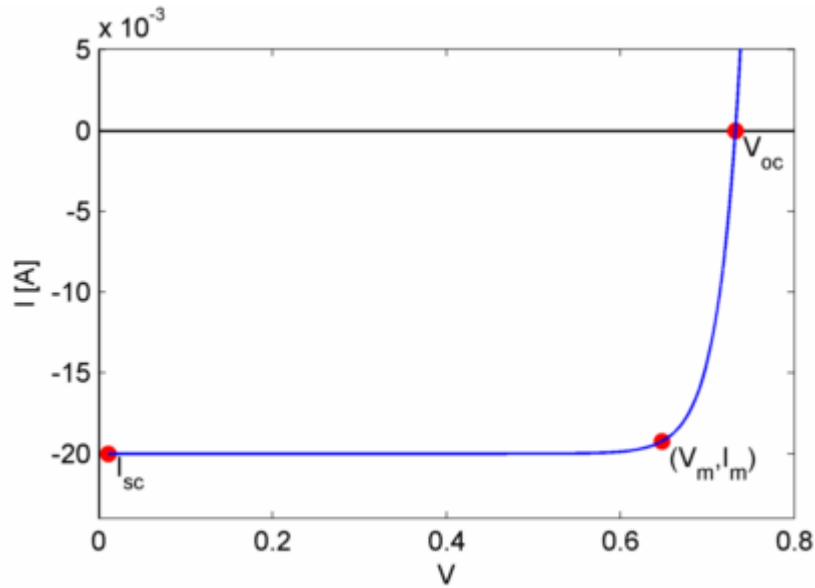


Figure 2: Typical IV curve of a solar cell.

Short circuit current

This is the amount of current flowing between the two poles when no bias is applied, and under normal conditions. If resistive effects are neglected and total collection is assumed, this is identical to the photogenerated current and presents an upper bound for the amount of current we can extract at any applied bias. It is a good metric regarding carrier generation performance, taking optical parameters such as absorption coefficient and bandgap engineering into consideration.

Open circuit voltage

To be able to extract any power from the device, each generated and collected electron also need to possess some potential energy. The open circuit voltage is defined as the voltage difference between the positive and negative sides of our solar cell under an infinite load. Under these circumstances the cell is under thermal equilibrium and the forward current over the junction exactly balances the light generated current. Since the forward current over the junction is exponential in respect to the applied bias, according to the ideal diode law, a higher light generated current will only slightly (logarithmically) affect V_{oc} :

$$V_{oc} = \frac{nk_B T}{q} \ln \left(\frac{I_L}{I_o} + 1 \right) \quad (1)$$

where n is the diode ideality factor, k_B is the Boltzmann constant, T is the temperature, q is the electron charge, I_L is the light generated current and I_o is the dark saturation current. The dark saturation current describes the diode leakage and is directly related to the amount of recombination in the device [2].

Expression (1) is based on a single-diode model where no resistive losses or leakage shunts are taken into consideration (see below), but gives a reasonably good picture of the relationship.

The open circuit voltage in a pn-junction is positively related to the bandgap of the material where the carriers are generated. Since the short-circuit current decreases with an increasing bandgap (fewer absorbed photons), they are contrary targets. Hence, there will be an optimum material for a given spectrum of incident light.

Fill Factor

The Fill Factor (FF) is defined as the ratio between the maximum power we can extract, to the product of the short circuit current (I_{sc}) and the open circuit voltage (V_{oc}):

$$FF \equiv \frac{V_m I_m}{V_{oc} I_{sc}} \quad (2)$$

and is a key parameter because it determines how much resistive and shunt path leakage losses we have in the cell. V_m and I_m are the voltage and current respectively, at the *maximum power point*, which is the point where their product (power) is the greatest (see figure 2).

Efficiency

The most important parameter used to define the performance of a solar cell is the efficiency factor η , which is the ratio between the maximum electrical output power and the incident solar power P_{in} :

$$\eta \equiv \frac{V_m I_m}{P_{in}} \quad (3)$$

The incident solar power is calculated based on the standardized Air Mass 1.5G data. This spectrum is the intensity per wavelength for solar irradiation at a zenith angle of 48.19 degrees, and corresponds to a total of 100 mW/cm² at the surface of the earth. It includes both direct and diffuse radiation [2].

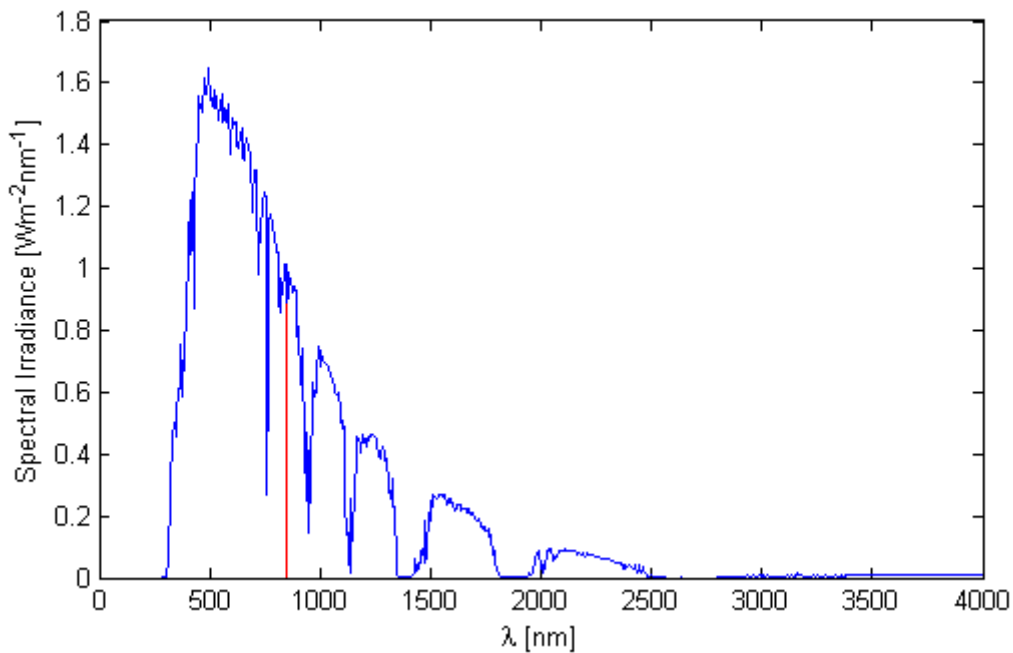


Figure 3: Air Mass spectrum 1.5G. The red line is at 843 nm, which is the wavelength-equivalent of the bandgap of CdTe (1.47eV). The drops in the curve are due to absorption by atmospheric gases [2].

1.3.2 Equivalent circuit

Any photovoltaic device could in principle be described by the following equivalent circuit diagram:

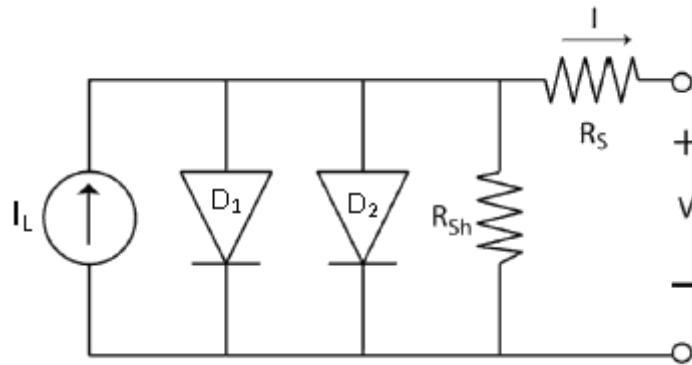


Figure 4: The double-diode equivalent circuit model.

consisting of a current source (I_L) modeling the photogenerated current, two diodes in parallel describing the diode characteristics for low bias and high bias respectively, a series resistor modeling series resistance effects in the material, and a parallel shunt resistor.

The current source could accurately describe the photogenerated current, if this current is independent of applied voltage. This holds true if the *superposition principle* is valid. This principle states that the output current from the cell at a given voltage can be regarded as a sum of the photocurrent I_L and the corresponding current measured in the dark. This assumes that the photocurrent is voltage-independent, which is not true for some devices. The advantage of its validity is that characterization of the cell can be reduced to a description of the short-circuit current under illuminated conditions, together with the current-voltage dependence studied under dark conditions, where I_L is zero [3]. By simulating and analyzing how and where most of the recombination takes place in the structure, it is also possible to optimize key parameters such as collection efficiency and open circuit voltage.

The low bias diode D_1 is supposed to model the dominant current transport mechanisms when a small external load is applied to the cell. In this region, most carriers are recombining in the depletion region and the diode has an ideality factor of two. This could qualitatively be seen as a less steep curve in a plotted $\log(I)$ - V diagram.

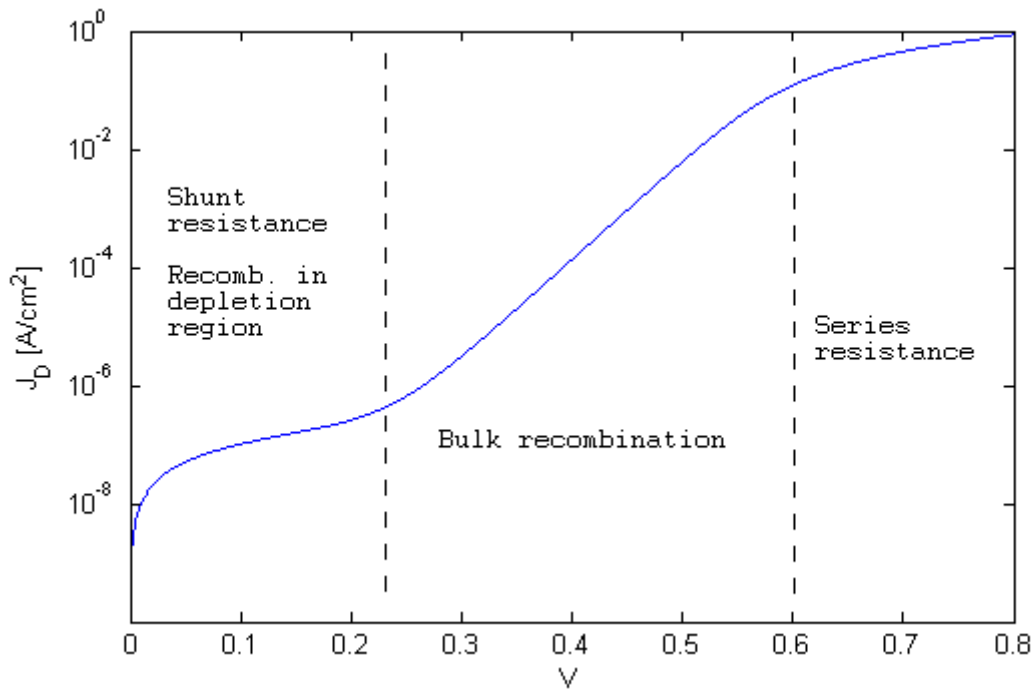


Figure 5: Typical semilogarithmic IV-curve for a solar cell under dark conditions.

The second diode D2 will mainly be important in the middle- to high-bias region, and models recombination currents in the bulk region of the materials. The ideality factor of this diode is one.

A series resistance R_S needs to be included to accurately take into account effects such as contact and metallization resistances, emitter sheet resistance and bulk resistance. A low series resistance is of importance since it allows for a greater current throughput at high bias, where most power is produced, and thereby increasing the fill factor and power conversion efficiency of the cell (see figure 6 left).

Experimentally, there will always be leakage currents that make their way past the junction, thus minimizing the charge separation capabilities of the cell. The shunt resistance R_{SH} in the diagram models these adverse currents and it is a necessity to keep this resistance as high as possible since leakage currents severely degrades the fill factor and thus the maximum power output of the device (see figure 6 right).

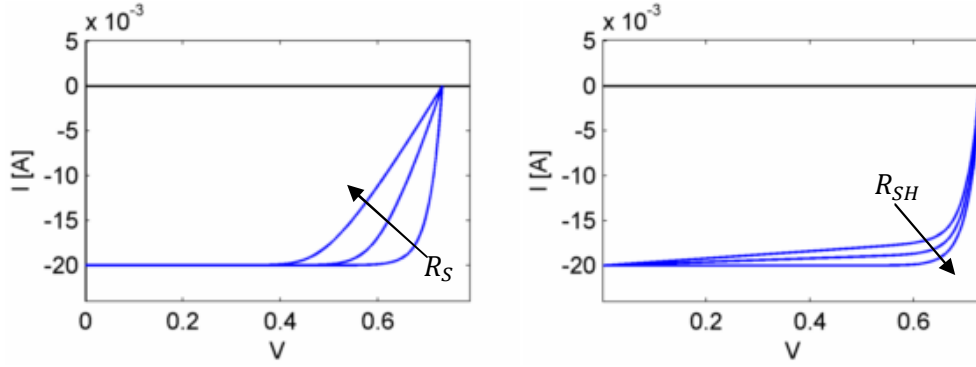


Figure 6: Effect of series (left) and shunt resistance (right). The series resistances are 0, 5 and 10 Ω with the corresponding fill factors 0.85, 0.72, 0.60 respectively. The shunt resistances are 250 Ω , 500 Ω and infinite with the corresponding fill factors 0.74, 0.79, 0.85.

By applying nodal analysis on the circuit model (figure 4), a compact expression for the extracted current density I under illuminated conditions is derived as

$$I = I_L - I_{01} \left(e^{\frac{q(V+IR_S)}{k_B T}} - 1 \right) - I_{02} \left(e^{\frac{q(V+IR_S)}{2k_B T}} - 1 \right) - \frac{V + IR_S}{R_{SH}} \quad (4)$$

where I_{01} and I_{02} is the saturation current density for the two respective diodes, q is the electron charge, k_B is the Boltzmann constant, T is the temperature and V is the applied bias.

1.4 Nanowire-based solar cells

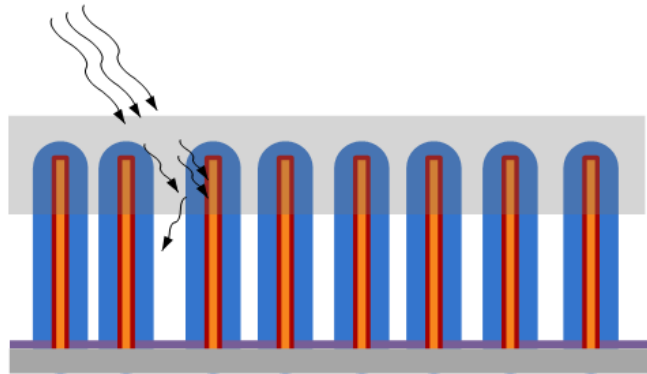


Figure 7: Cross section of a nanowire array, side view. The arrows indicate incident and scattered photons, the blue area is the outer shell layer with absorber material, and the yellow area is the inner core with collector material. The red area indicates the junction between the core- and shell part. The top gray area is a transparent contact material, and on the bottom there is a back contact material (gray) and an insulating material (purple).

1.4.1 Advantages

There are mainly two reasons for building solar cells with nanowire arrays, compared to the conventional planar geometry (wafer/thin-film). These advantages can mostly be seen as a possibility for lower material quantity and higher defect tolerance, thus reducing cost.

The first advantage is that of light trapping. One of the biggest losses in solar cells is already at the optical stage in the form of reflection at the top and transmission through the cell. Therefore, it is of great significance to decrease these effects in order to keep most of the photons within the structure and giving them further chances of exciting an electron from the valence band to the conduction band and thus being useful. This is called *light-trapping*, and the very nature of a nanowire array allows for a high amount of photon scattering in the structure, without the need for additional light-trapping mechanisms such as random surface texturing [4].

The second advantage that comes into play is the separation of two conflicting phenomena. A solar cell consisting of an array of radial nanowires parallel to the incident sunlight will solve an unavoidable compromise in planar devices: the absorption layer should be thick enough to absorb as many photons as possible, but at the same time thin enough (see 2.3 Recombination) for optimum collection efficiency. A core/shell structured nanowire decouples these requirements since it can be as long as necessary for effective absorption, but simultaneously having a sufficiently thin shell layer for good collection of generated carriers [5].

1.4.2 ZnO/CdTe core shell nanowires

In our specific case, we are implementing a staggered (type II) heterojunction consisting of CdTe as the absorbing outer shell layer, and ZnO as the collecting inner core part.

Cadmium telluride (CdTe) is an excellent absorber since it has a high absorption coefficient ($>10^5 \text{ cm}^{-1}$) due to a direct bandgap of around 1.50 eV that is well-matched to the solar irradiation spectrum.

The reason Zinc oxide (ZnO) is used as the inner collector of the nanowire, is that it is easy to grow by many different types of methods, is cheap, abundant, radiation resistant and non-toxic [6][7][8]. It is

an n-type semiconductor, where excess Zn acts as donor impurities. The degree of doping can be varied by making a suitable choice of parameters during the deposition process [9]. It also has a suitable band structure that in conjunction with CdTe will result in a heterojunction at the interface between the two materials (see figure 8). This heterojunction will in theory be able to separate electrons from holes without any doping [10].

The core/shell nanowire growth process can be done through chemical bath deposition and close space sublimation. This synthetisation technique will produce a CdTe shell consisting of nanograins, and has been shown to produce an interface without any epitaxial relation between the two semiconductors. This prevents that any strain due to lattice mismatch will occur, and should thus make the compound free from nucleation of dislocations through strain relaxation [7].

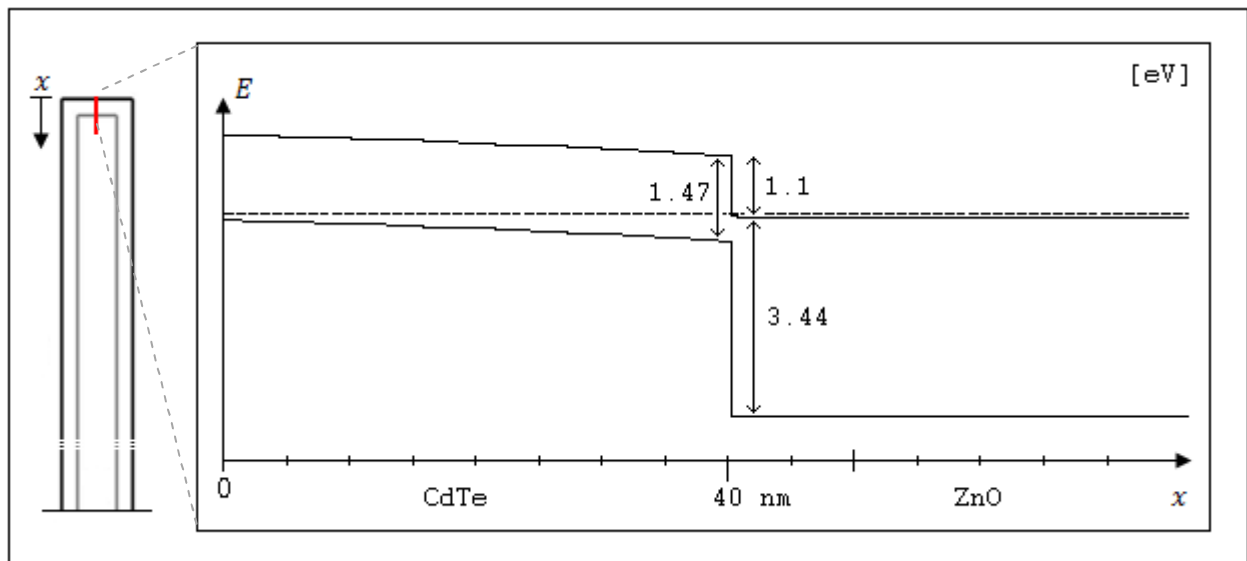


Figure 8: Energy band diagram over the heterojunction at the interface between CdTe and ZnO.

2. Theory

In this chapter I will give a brief introduction to the underlying physics that govern the electrostatic behavior and charge transport processes in a semiconductor. The device simulator being used, Sentaurus TCAD, retains the ability to model all of them.

2.1 The Poisson and continuity equations

These are the two most central equations that form the very basis of the theory that describes the electrical behavior in a semiconductor device, and their consideration is imperative for accurate modeling.

The electrostatic potential at a given point is governed by Poisson's equation

$$\nabla^2 \varphi = -\frac{\rho}{\epsilon} \quad (5)$$

which relates the electrostatic potential φ to the charge density ρ and the electrical permittivity ϵ of the medium. The charge density is the sum of all charge densities, both mobile (electrons n and holes p) and fixed (ionized donor N_D and acceptor atoms N_A):

$$\rho = q(p - n + N_D - N_A) \quad (6)$$

The charge densities of the mobile electrons and holes are expressed by the continuity equations

$$\nabla \cdot J_n = q(U + \frac{\partial n}{\partial t}) \quad (7)$$

$$\nabla \cdot J_p = -q(U + \frac{\partial p}{\partial t}) \quad (8)$$

that describes charge conservation by relating the change of carrier concentration over time to the net rate of generation/recombination processes (U) and the divergence of the current density ($\nabla \cdot J_{n,p}$).

Each charge carrier transport mechanism has a specific current density expression, and in the following two sections I will describe three of them, along with a common generation/recombination process.

2.2 Transport mechanisms

2.2.1 Drift/diffusion

The two most considered physical processes that govern charge carrier movement in a semiconductor are *drift* and *diffusion*. The drift/diffusion-model is also the default transport model in Sentaurus TCAD.

Drift

When no electric field is applied, every free moving electron in the conduction band is scattering randomly between collisions with atoms and scattering centers in the crystal lattice. Over time, since the scattering directions are random, the net movement is zero. If an electric field \mathcal{E} is applied, this will induce a force $-q\mathcal{E}$ on each electron. This force accelerates them in the opposite direction to the

field in between each collision. By assuming that all the gained momentum during the time between collisions is lost in each collision, we can obtain the net *drift* velocity over time:

$$-q\mathcal{E}\tau_c = m_n v_{drift,n} \rightarrow v_{drift,n} = -\frac{q\tau_c}{m_n} \mathcal{E} \quad (9)$$

where q is the electron charge, τ_c is the time between collisions (also called *mean free time*), m_n is the *effective* mass of the electron and \mathcal{E} is the electric field. The effective mass is the apparent mass a free-moving electron has in a crystal lattice (this also applies to holes, with an effective mass m_p). The product $q\tau_c/m_n$ is called the *mobility* (μ_n) of the electron, and is a material parameter that describes how easily an electric field can affect its velocity. We can derive the same kind of expression for holes in the valence band, but without the minus sign (since holes have a positive charge) and with the hole effective mass instead.

The current density (charge per unit time and unit area) due to this drift of electrons and holes is obtained by multiplying the drift velocity ($v_{drift,n}$ and $v_{drift,p}$) with the carrier concentration (n and p) and the charge ($-q$ and q) for them both, and summing them:

$$J_{drift,n} = -qn v_{drift,n} = q\mathcal{E}n\mu_n \quad (10)$$

$$J_{drift,p} = qp v_{drift,p} = q\mathcal{E}p\mu_p \quad (11)$$

Diffusion

If the concentration of electrons is higher in one place than in another, they tend to move from the high density region towards the low density region through a diffusive process. In one dimension, this can be calculated into a current component by considering the random movement of electrons at one mean free path l away at the right and left side of any given spatial point, which is set to $x=0$ (see figure 9). In one dimension, the probability of one electron randomly moving from l or $-l$ to 0 is 50%.

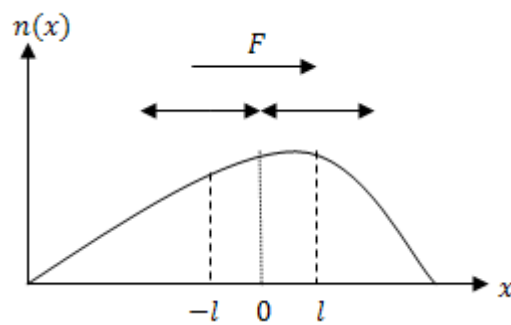


Figure 9: The rate of electron movement (F) over an arbitrary point $x=0$ is depending on the electron concentration (n) one mean free path (l) before and after this point.

If we suppose that all points have the same temperature (the same thermal velocity v_{th}), an expression for the net rate F of electrons moving over $x=0$ from left to right is:

$$F = 0.5 \cdot n(-l) \cdot v_{th} - 0.5 \cdot n(l) \cdot v_{th} = 0.5 \cdot v_{th} \cdot (n(-l) - n(l)) \quad (12)$$

If the electron concentration n is approximated by a Taylor expansion of two terms around $x=0$:

$$n(x) \approx n(0) + \frac{dn}{dx}x \quad (13)$$

then equation 12 will be

$$F = -v_{th}l \frac{dn}{dx} \quad (14)$$

where the product $v_{th}l$ is called the *diffusion coefficient* D and it describes how fast the charge carrier concentration is changing under the influence of a concentration gradient.

The diffusion current density equations for electrons and holes are then simply the product of their respective charge ($-q$ for electrons and q for holes) and their rate of diffusion:

$$J_{diff,n} = -qF_n = qD_n \frac{dn}{dx} \quad (15)$$

$$J_{diff,p} = qF_p = -qD_p \frac{dp}{dx} \quad (16)$$

where D_n , D_p , n , and p are the diffusion coefficients and concentrations for electrons and holes respectively. The reason that we add a minus sign to the hole diffusion current, is that its reference direction is opposite to the electron current.

The drift and diffusion terms can then be aggregated into the total carrier density equations:

$$J_n = J_{drift,n} + J_{diff,n} = q(\mathcal{E}n\mu_n + D_n \frac{dn}{dx}) \quad (17)$$

$$J_p = J_{drift,p} + J_{diff,p} = q(\mathcal{E}p\mu_p - D_p \frac{dp}{dx}) \quad (18)$$

Since both the mobility and the diffusion coefficient basically depends on the same physics, carrier interactions and scattering within the medium atoms, a relationship between them exists, called the *Einstein Relation* [11]:

$$D = k_B T \mu / q \quad (19)$$

which is derived based on the theorem for equipartition of energy

$$\frac{mv_{th}^2}{2} = \frac{3}{2} k_B T \quad (20)$$

stating that each degree of freedom (three, one per dimension in space) contributes $k_B T/2$ to the kinetic energy of a carrier. The Einstein relation is valid under most circumstances. But, if for example the doping gradient is steep, it fails to hold and the transport mechanism is said to exhibit non-Einstein diffusivity [12].

2.2.2 Thermionic emission

In the derivation of the classical ideal diode equation, only the collective diffusive forces are assumed to contribute to the transport against the electric field and the energy distribution of carriers is

approximated as a delta function by the conduction- and valence band edge for electrons and holes respectively.

If the carrier concentration is low, or if the material interface poses a barrier that is too steep, diffusion ceases to be the dominant transportation mechanism and the individual momentum of each carrier has to be considered. When the concept of thermionic emission is used to describe carrier transport over a metal-semiconductor barrier, it is generally called Schottky theory.

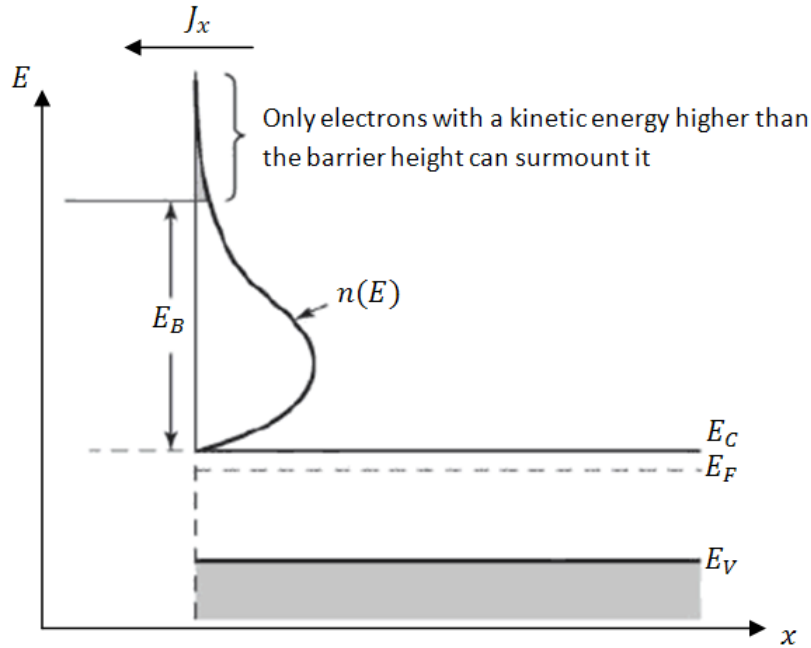


Figure 10: Energy band diagram, picturing the electron density per energy $n(E)$ just before the barrier. E_B is the barrier height, E_C is the lower edge of the conduction band, E_V is the top edge of the valence band, E_F is the Fermi level, J_x is the thermionic current density.

The thermionic emission current is determined by considering the density of electrons that has enough velocity towards the barrier to surmount it. We do this by integrating the density of electrons that has an energy higher than the barrier height E_B , with their velocity v_x towards the barrier, and the electron charge q :

$$J_x = q \int_{E_B}^{\infty} v_x(E) n(E) dE \quad (21)$$

The electron density for a given energy $n(E)$ is the product of the density of states $N(E)$ with the occupational probability $F(E)$ which can be approximated with the Boltzmann distribution since the Fermi level E_F usually is far more than $3k_B T$ below the top of the barrier.

$$\begin{cases} N(E) = \frac{8\pi\sqrt{2}}{h^3} m_n^{3/2} \sqrt{E} \\ F(E) = \exp\left(\frac{-(E - E_F)}{k_B T}\right) \end{cases} \longrightarrow n(E) dE = \frac{8\pi\sqrt{2}}{h^3} m_n^{3/2} F(E) \sqrt{E} dE \quad (22)$$

We can rewrite the last part of the equation as a function of velocity instead:

$$E = \frac{m_n v^2}{2} \Rightarrow \sqrt{E} dE = \frac{m_n^{3/2}}{\sqrt{2}} v^2 dv \quad (23)$$

so that the current density equation (eq. 21) now becomes:

$$J_x = \frac{2qm_n^3}{h^3} \exp\left(\frac{E_F}{k_B T}\right) \int_{v_0}^{\infty} v_x \exp\left(-\frac{m_n v^2}{2k_B T}\right) \cdot 4\pi v^2 dv \quad (24)$$

where v_0 is the minimum velocity required to surmount the barrier.

This is essentially a volume integral over a sphere, and if we consider the velocity as a vector in space, $v = (v_x^2 + v_y^2 + v_z^2)^{1/2}$, and only integrate over v_x -components that is greater than what is required to overcome the barrier, eq. 24 becomes:

$$J_x = \frac{2qm_n^3}{h^3} \exp\left(\frac{E_F}{k_B T}\right) \int_{v_{x0}}^{\infty} v_x \exp\left(\frac{-m_n v_x^2}{2k_B T}\right) dv_x \int_{-\infty}^{\infty} \exp\left(\frac{-m_n v_y^2}{2k_B T}\right) dv_y \int_{-\infty}^{\infty} \exp\left(\frac{-m_n v_z^2}{2k_B T}\right) dv_z \quad (25)$$

which is readily solvable by noting that the last two integrals are Gaussian, yielding:

$$J_x = \frac{2qm_n^3}{h^3} \exp\left(\frac{E_F}{k_B T}\right) \exp\left(\frac{-m_n v_{x0}^2}{2k_B T}\right) \frac{k_B T}{m_n} \sqrt{\frac{2\pi k_B T}{m_n}} \sqrt{\frac{2\pi k_B T}{m_n}} \quad (26)$$

And by finally rewriting v_{x0} back into its corresponding energy through $E_B = \frac{m_n v_{x0}^2}{2}$, we have:

$$J_x = \frac{4\pi q m_n k_B^2}{h^3} T^2 \exp\left(\frac{E_F - E_B}{k_B T}\right) \quad (27)$$

The first factor $4\pi q m_n k_B^2/h^3$ is called the *effective Richardson constant* A^* , and is equal to 120 A/cm²/K² in vacuum.

Equation 27, also called Richardson's law, assumes that the electrons has the same effective masses in both semiconductors, that we have a thermal equilibrium condition, and it also does not consider electron flow in the opposite direction. A more thorough thermionic current density equation that describes the interface condition of a heterojunction and includes these parameters is [13]:

$$J = A_2^* T^2 \eta \left\{ \exp\left(\frac{E_{Fn2} - E_{C2}}{k_B T}\right) - \exp\left(\frac{E_{Fn1} - E_{C1} - E_B}{k_B T}\right) \right\} \quad (28)$$

where A_2^* is the effective Richardson constant of semiconductor #2, E_{Fn1} and E_{Fn2} are the quasi-Fermi levels for electrons in both materials, E_{C2} and E_{C1} are the conduction band energy levels for the materials (see figure 11), and η is a correction term that takes into account the difference in effective masses $m_{n1,n2}$:

$$\eta = 1 - \left(1 - \frac{m_{n1}}{m_{n2}}\right) \exp\left(\frac{-E_B}{\left(1 - \frac{m_{n2}}{m_{n1}}\right) k_B T}\right) \quad (29)$$

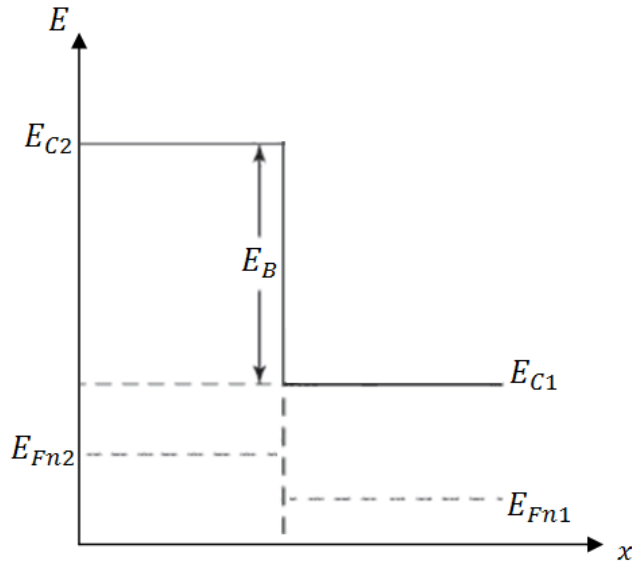


Figure 11: Band diagram and parameters for the extended thermionic emission model described in eq. 28 and 29.

2.2.3 Tunneling

Quantum mechanical effects, such as tunneling, are becoming increasingly important to take into consideration when simulating electronic devices today. As dimensions grow smaller, the space distribution of probability wave functions for neighboring states overlap to a significant amount and cannot be neglected. This has led to the development of several transport models with the aim of accurately describing quantum mechanical tunneling of carriers [14].

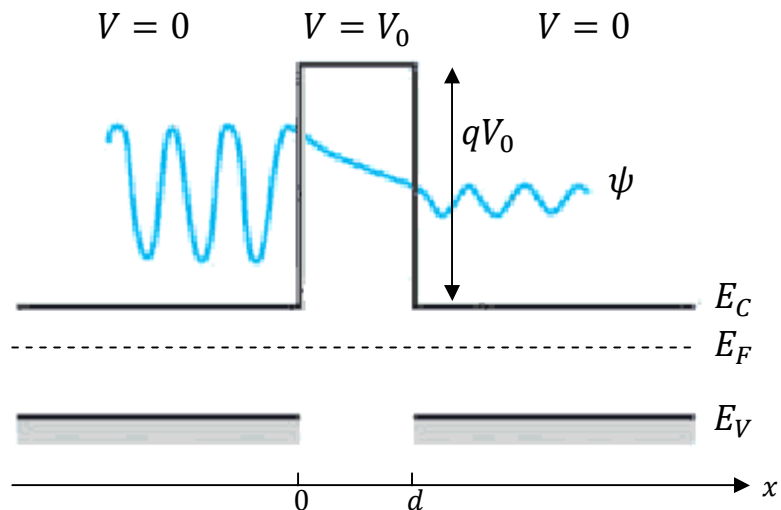


Figure 12: Band diagram including a barrier, displaying how the wavefunction (blue) is affected.

In steady state, the behavior of conduction electrons travelling through the semiconductor crystal lattice can in one dimension be described by the time-independent Schrödinger equation:

$$-\frac{\hbar^2}{2m} \frac{d^2\psi(x)}{dx^2} + qV(x)\psi(x) = E\psi(x) \quad (30)$$

where \hbar is the reduced Planck constant $\frac{h}{2\pi}$, m is the effective mass of the electron, $qV(x)$ is the potential energy relative to the conduction band edge E_C , E is the kinetic energy, and $\psi(x)$ is the wave function at position x .

If we consider a movement of electrons from left to right (see figure 12), the solutions to eq.30 in the regions before, inside and after a barrier of thickness d are:

$$\psi(x) = \begin{cases} A\exp(ik_1x) + B\exp(-ik_1x) & x \leq 0 \\ F\exp(k_2x) + G\exp(-k_2x) & 0 \leq x \leq d \\ C\exp(ik_1x) & x \geq d \end{cases} \quad (31)$$

where $k_1 = \sqrt{2mE}/\hbar$ and $k_2 = \sqrt{2m(qV_0 - E)}/\hbar$ are the wavenumbers for the regions outside and inside of the barrier respectively. Since the wavefunction must be continuous, it has to be equal at both sides of each boundary. This gives us relations between the coefficients A, B, C, F and G. Since A and C can be considered as the amplitude of the incident and transmitted wavefunctions, we can determine the probability of an electron to be transported across the barrier, called the *transmission coefficient* [11]:

$$T = \left(\frac{C}{A}\right)^2 = \left[1 + \frac{(qV_0 \sinh(k_2d))^2}{4E(qV_0 - E)}\right]^{-1} \sim \exp(-2k_2d) \quad (32)$$

Due to this negatively exponential relationship between tunneling distance and transmission probability, tunneling currents will mainly have a significant contribution under high ($>10^6$ V/m) fields (band-to-band tunneling) or when there is a high density of defect states within the band gap.

If the tunneling process through a barrier is aided by defect states in the band gap, it is called *Trap-Assisted Tunneling* (TAT). Figure 13 demonstrates an example of how a TAT-process can act as a charge carrier transfer mechanism over a heterojunction, where an electron tunnels (A) from the conduction band to a defect state in the band gap of the other semiconductor, and then recombines (B). This can play a major role and be the dominant transport process at the interface when the barrier is too high for any significant thermionic current to occur [6].

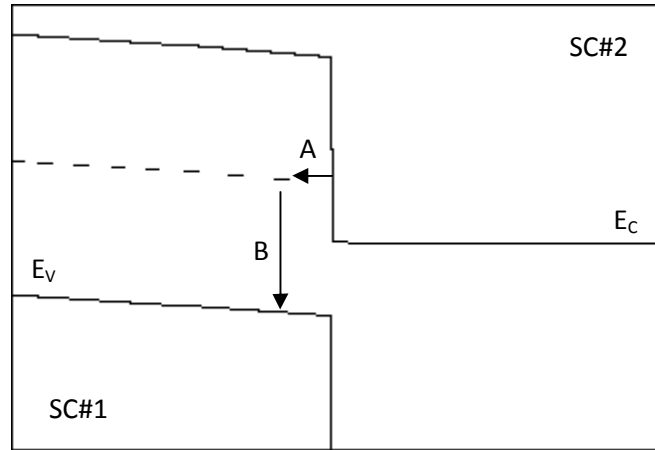


Figure 13: Example of Trap-Assisted Tunneling. An electron tunnels (A) from the conduction band of semiconductor#2 (SC#2) to a trap located in the middle of the bandgap for semiconductor#1 (SC#1) and recombines (B) to the valence band of SC#1.

Several compact tunneling models exist for both direct and trap assisted tunneling, which can give an approximate explanation for the measured current-voltage characteristics without the involvement of computationally expensive integrations. For a simulator that is aware of the physical parameters at each mesh point, however, it is better to model the tunneling process as a net recombination term in the continuity equations (eq. 7,8) [14].

2.3 Recombination

Under thermal equilibrium, the total generation rate is equal to the recombination rate and the *mass action law* $n_i^2 = np$ is maintained. When excess minority carriers are introduced into the system, for example by optical generation, through contacts or injection over the junction, they have a limited time they can spend before encountering a majority carrier and recombine. The average of this time is called the *minority carrier lifetime* τ , and the recombination rate R is thus $\delta n/\tau$ (where δn is the excess minority carrier concentration) [2]. This is a very important thing to consider in solar cells, since whenever a generated electron-hole-pair fails to be separated by the junction and instead recombine again, the potential energy of the excited electron is “lost” through lattice heating (nonradiative) or photon emission (radiative).

The average *length* that a minority carrier diffuses before recombining is called the *minority carrier diffusion length*:

$$L = \sqrt{D\tau} = \sqrt{v_{th}l\tau} = \sqrt{kT\mu\tau/q} \quad (33)$$

where the last equation is valid if the Einstein relation (eq.19) holds. Since we want as many generated carriers as possible to diffuse to the junction and be collected, it is of high importance to design the absorption layer thickness so that it does not exceed the minority carrier diffusion length. As can be observed in eq. 33, this critical thickness is dependent on temperature, choice of semiconductor and the minority carrier lifetime.

Lattice dislocations and impurity atoms, such as gold, play a crucial role when it comes to carrier recombination. These *recombination centers* or *traps* are able to briefly capture an electron or a hole and thereby increasing the probability for it to recombine. When the recombination process is through localized defect states in the band gap, it is called *indirect* recombination. Since an impurity

atom is only active as a trap when it is not ionized, it is most effective when it is as far from the band edges as possible (in the middle of the band gap). When a defect state is located more than $3kT$ from either band edges, it is called a *deep* defect state [13].

If we consider only one defect level, located at an energy E_t in the band diagram, an expression for the net recombination rate U is given by the *SRH* (Shockley-Read-Hall) formula [11]:

$$U = \frac{v_{th}\sigma_n\sigma_p N_t (np - n_i^2)}{\sigma_n \left(n + n_i \exp\left(\frac{E_t - E_i}{kT}\right) \right) + \sigma_p \left(p + n_i \exp\left(-\frac{E_t - E_i}{kT}\right) \right)} \quad (34)$$

where v_{th} is the electron thermal velocity, σ_n and σ_p is the capture cross-section for electrons and holes respectively, N_t is the defect density, $np - n_i^2$ is the excess minority carrier concentration, n and p is the electron and hole concentration respectively, n_i is the intrinsic carrier concentration, E_t is the defect energy level, $E_i = (E_c + E_v)/2$ is the intrinsic Fermi level, k is the Boltzmann constant and T is the temperature.

If the electron and hole capture cross sections are equal, the highest net recombination rate is exhibited when the defect state is exactly in the middle of the band gap.

An extension of the conventional SRH recombination mechanism, where two defect levels are involved, is called *Coupled Defect Level* [12].

2.4 Temperature dependence

In the drift-diffusion current density equations (17, 18), three variables have a temperature dependency [15]. First, we can consider the carrier concentration. In the extrinsic temperature region of a doped semiconductor, all dopant impurities ($N_{A,D}$) are ionized and the concentration of these are much higher than for the thermally generated carriers (n_i). Within this temperature region, the majority carrier concentration remains almost stable and depends solely on the amount of doping (see figure 14). Before and after this region, it increases exponentially with temperature. The other two parameters that depend on temperature are the mobility and the diffusion coefficient. For low to medium impurity concentrations, the mobility is mainly limited by lattice scattering and decreases with temperature. The diffusion coefficient increases with temperature since the thermal velocity of the charge carriers is higher, thus increasing the speed at which they diffuse [11].

In conclusion, we see that the current increases with temperature if the electric field is low since the transport then is dominated by diffusion. If we have a high electric field, the drift component will dominate and the current will decrease with temperature [15]. This conclusion is drawn with the assumption that we only consider majority carrier currents in the extrinsic temperature region.

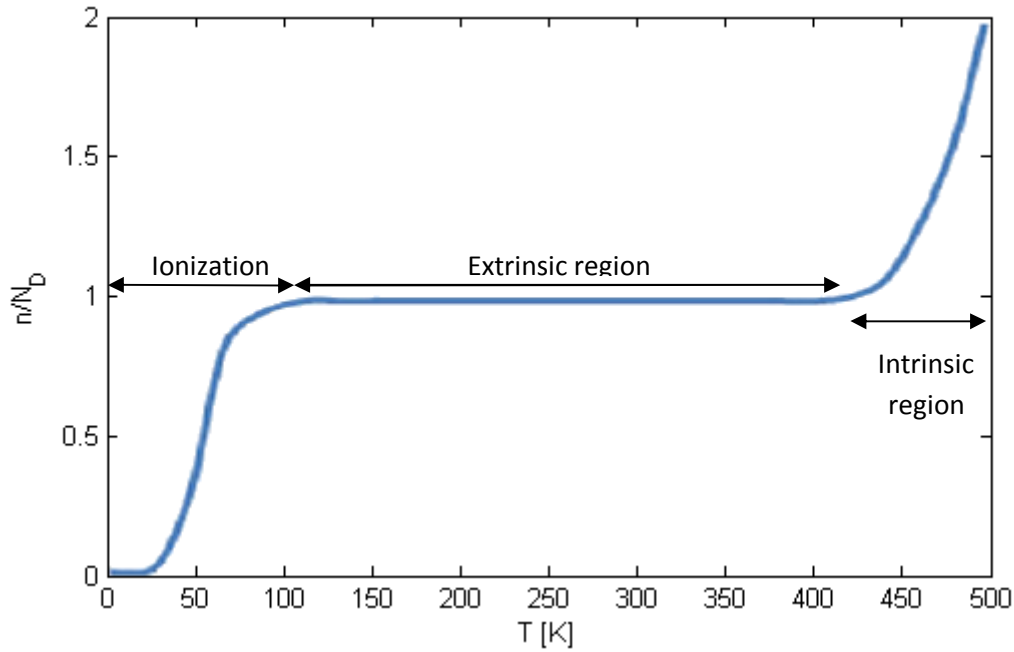


Figure 14: Ratio between the electron concentration and donor atom concentration with respect to temperature.

The temperature dependence for the current created by thermionic emission over a heterojunction barrier described by eq. 28 is demonstrated in figure 15. In this plot, the electron quasi-Fermi level is kept fixed at 0.9 and 0.1 eV to the left (E_{Fn1}) and right (E_{Fn2}) of the barrier respectively, in respect to the lower conduction band (E_{C1}). The barrier height (E_B) is incremented from 0.3 to 0.7 eV in steps of 0.1 eV.

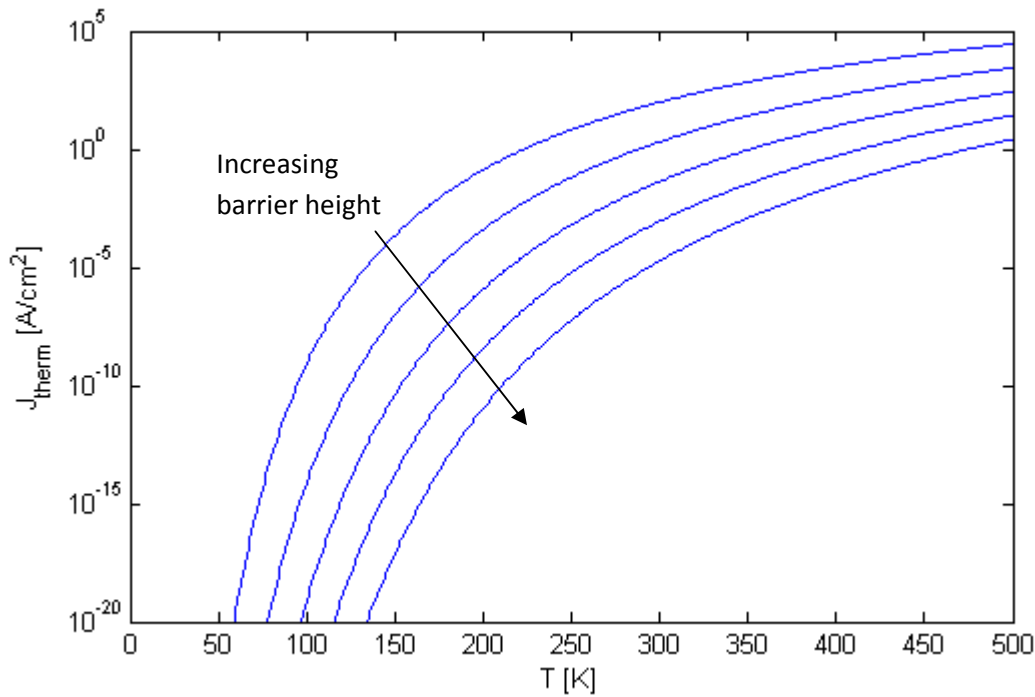


Figure 15: Temperature dependence for the thermionic emission current over a potential barrier in a heterojunction. The barrier height is increased from 0.3 to 0.7 eV, in steps of 0.1 eV.

Regarding the tunneling current, we can have a look at equation 32. If we denote the kinetic energy of the carriers as $1.5kT$, we can get a qualitative relationship between the system temperature and the probability for a carrier to be transmitted through a square barrier. In figure 16, the tunneling coefficient is plotted as a function of temperature. The barrier height is incremented in steps of 0.1 eV, from 0.3 to 0.7 eV. The tunneling distance is 1 nm and the mass is the electron mass in vacuum. Noteworthy, the coefficient only increases with a factor of about three between 100 and 300 K. Since the current transmitted through tunneling is directly proportional to the transmission coefficient (given an infinite supply of electrons), this can be put in contrast to the thermionic emission current increase of several orders of magnitude in the same temperature range.

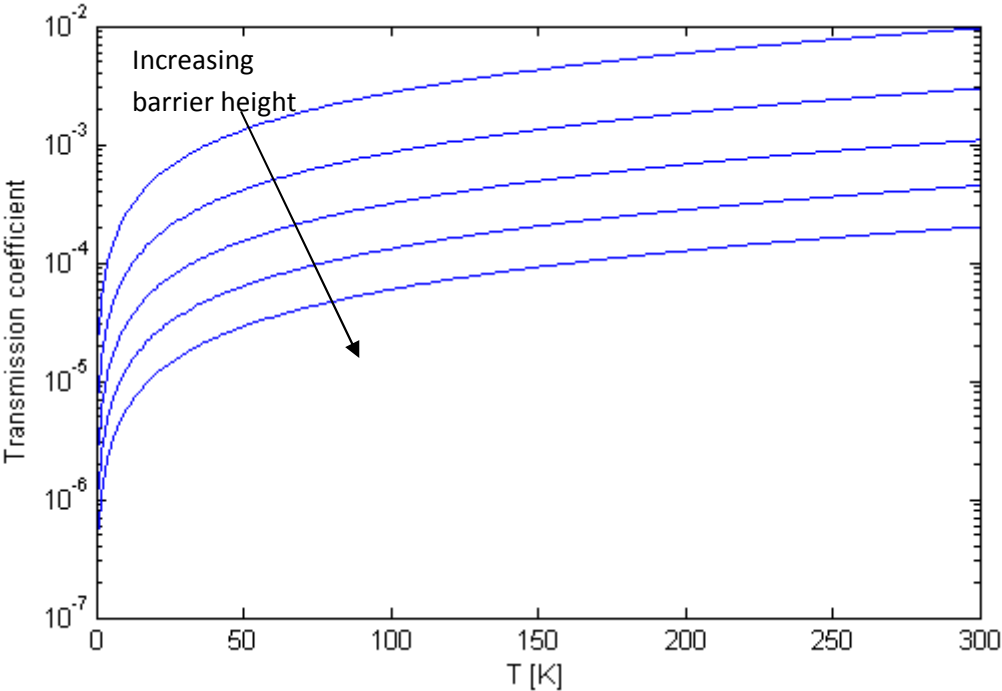


Figure 16: Transmission coefficient for tunneling through a 1 nm wide square potential barrier. The barrier height is increased from 0.3 to 0.7 eV, in steps of 0.1 eV.

It is worth to note that the current through a semiconductor device governed by several sequential transport mechanisms, is limited by the process with the lowest charge carrier transfer rate.

3. Method

3.1 Simulation

Technology Computer Aided Design (TCAD) software started to emerge during the 1960's, and has today evolved into an essential part in the development of novel semiconductor devices. They are very useful during the design stage of semiconductor device development because the time saving that could be achieved in comparison to real device fabrication is immense.

By numerical solving of the electrostatic potential distribution and charge carrier transport processes throughout the device, highly realistic simulation results can be achieved.

This is done by first dividing the structure into a grid of discrete points, a so called mesh, and then subsequently solving Poisson's equation (eq. 5) and the continuity equations (eq. 7, 8) for each mesh point.

These non-linear coupled partial differential equations are solved numerically through discretization into difference equations and then processed by a Newton-Raphson iteration technique.

The boundary conditions for the system of differential equations could be electrical or thermal. Electrical boundary conditions are called the *contacts* or *electrodes* of the device and can be defined as either Ohmic, Schottky or insulator type. Specification of thermal boundary conditions is necessary during simulations where temperature equations are considered.

Sentaurus is able to model the current densities in a number of different ways. The most common one, drift-diffusion, is applicable under normal circumstances with constant temperatures and low power densities [12]. This transport mechanism was employed in the bulk part of the semiconductors.

Since the CdTe/ZnO junction is heterogeneous, it is suitable to model the carrier transport at the interface as a thermionic emission process rather than drift-diffusion, since the quasi-Fermi levels can be discontinuous at the heterojunction [12].

In Sentaurus, tunneling processes are modeled as a *field enhancement* of the standard SRH-mechanism. Therefore, they are incorporated into the net recombination part of the continuity equation rather than the current density expression [12][14]. The model we chose is called *Dynamic Nonlocal Path Trap-assisted Tunneling* in conjunction with the *Hurkx* TAT model. It is dynamic in the sense that it does not require the construction of a special purpose tunneling-path mesh in beforehand. Instead, the tunneling trajectory is calculated for each

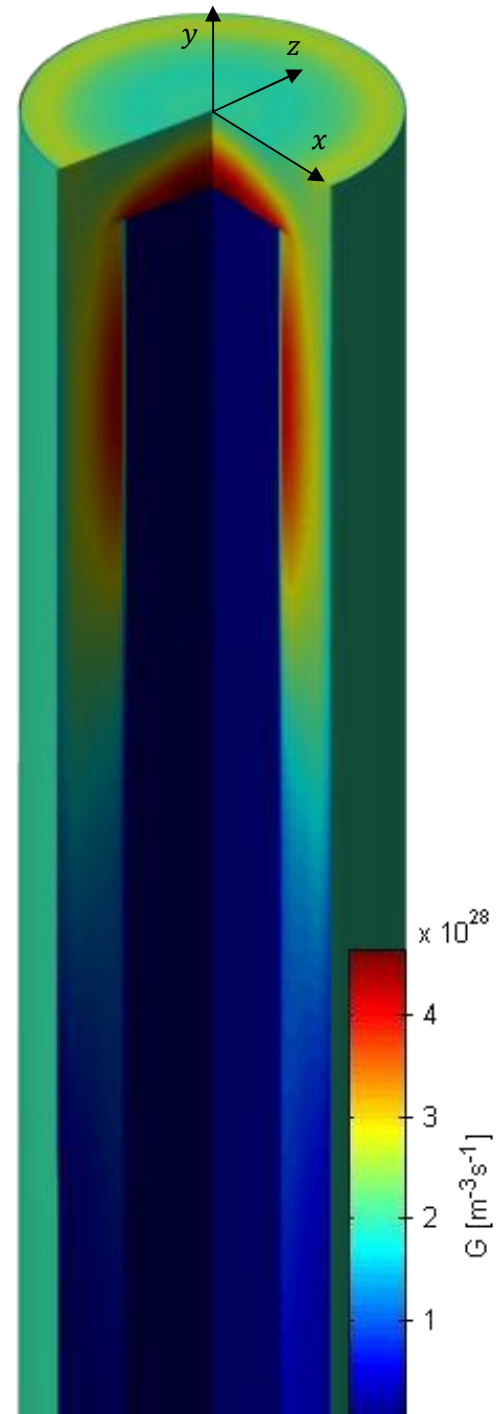


Figure 17: Cross section of the top part of the modeled nanowire. Red indicates an area with a higher optical generation rate.

mesh point based on the profile of the energy bands. It is called nonlocal because it actually models spatial transport of carriers, through the recombination and generation rate values at the beginning and the end of the tunneling path respectively. There are other *local* models that only affect the recombination rate at a fixed point depending on the surrounding electrical field. This model is advantageous when simulating tunneling through heterojunctions since the barrier profile is modulated by the material composition rather than the electrical field [12].

Since solar cells rely on the optical generation of carriers, this also has to be modeled and incorporated into the total generation rate. This can be done by a built-in optical solver, or read from a generation rate table produced by external software.

A highly optimized and fast optical transmission solver, called Aperiodic Fourier Modal Method (AFMM), has been developed at IMEP-LAHC. It is based around a solving method called Rigorous Coupled Wave Analysis (RCWA). As input, it takes a structure with varying refractive indices depending on material, along with a definition of the incident light intensity, spectrum and angle. The output is a table over the generation rate for each mesh point of the structure.

Based on previous work by Michallon et al [10], the optimal configuration of the array, in terms of ideal short-circuit density (every absorbed photon generates an electron which is collected), is with a square ordering, a period of 450 nm, a nanowire diameter of 180 nm, a CdTe shell thickness of 40 nm, and a height of 3 μm .

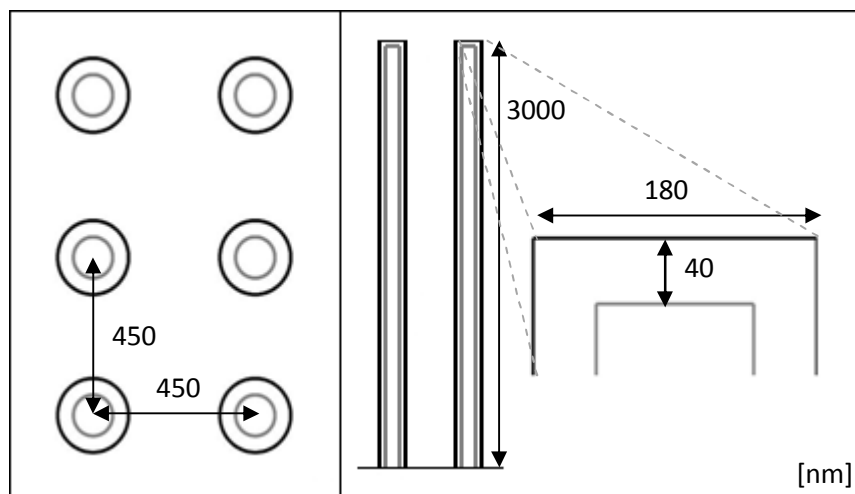


Figure 18: Top view of the array setup (left), and a cross-sectional side view of two nanowires including an enhancement over the top section (right).

Since the spatial resolution of the structure in the produced generation rate table is higher than the resolution of the mesh used by Sentaurus to perform the electrical simulations, a conversion from the former to the latter has to be performed. This was done with a specially developed Matlab script that searches for, and selects, the closest matching point in the optical generation table, for each point in the Sentaurus mesh. The resulting list is then incorporated into the Sentaurus mesh file as a separate data structure, including appropriate header objects.

As can be seen in figure 17, radial symmetry of the generation rate is assumed. The optical simulator will actually produce a full 3D dataset, but this is converted into a rotation plane around the y-axis by

taking the average around the perimeter at each radius. By performing the electrical simulations on the structure while exploiting this symmetry, significant reduction in computing time can be made.

To be able to evaluate the effectiveness of the nanowire array structure, we also did simulations on planar devices, where the thickness of the CdTe-layer was set to 297 nm and 40 nm. 297 nm corresponds to the same effective thickness as in the array setup. The same effective thickness means that both structures has the same volume of CdTe per given area of incident light.

Physical parameters employed in the simulations are listed in table 1.

	CdTe	ZnO
Band gap [eV]	1.47	3.44
Electron affinity [eV]	3.5	4.6
Relative permittivity	10.16	8.656
Electron effective mass [m_e]	0.0963	0.24
Hole effective mass [m_e]	0.35	0.59
Electron mobility [cm^2/Vs]	1100	200
Hole mobility [cm^2/Vs]	100	64
Electron lifetime [ns]	0.2	0.5
Hole lifetime [ns]	0.2	0.5

3.2 Measurements

Simulations are very useful in order to quantitatively see how the figures of merit vary in respect to physical parameters. In an attempt to validate our model, experimental dark current measurements were done on a planar structure containing CdTe on top of ZnO.

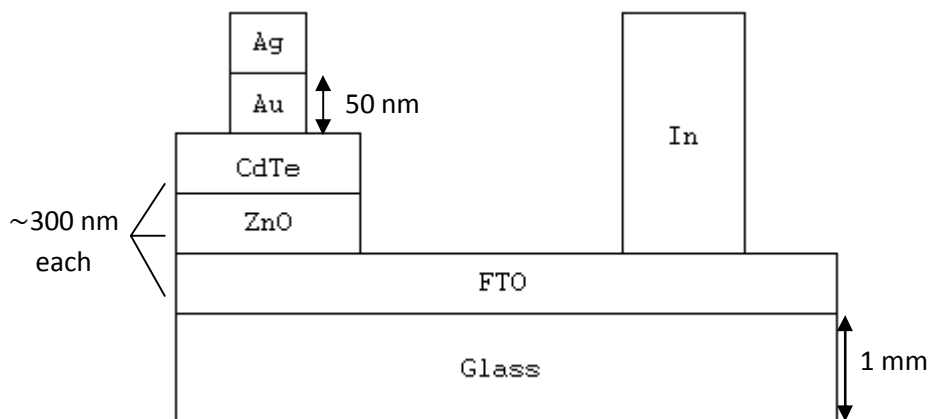


Figure 19: Test sample.

The test sample was prepared by first depositing a layer of fluorine doped tin oxide (FTO) on top of a 1 mm thick glass substrate through spray pyrolysis, with the FTO acting as a back contact. FTO is a material commonly used as a transparent contact material in solar cells. Then, a layer of ZnO was applied with chemical bath deposition, followed by close space sublimation of CdTe. To be able to reach the underlying FTO back contact, a part of the ZnO-CdTe layer was removed by etching in nitric

acid. The top contact material was chosen to be gold, and a 50 nm thick layer was evaporated through a mask on top of the CdTe. To assure that the probes were in good contact with the sample, and to avoid scratching or punching through the thin layers with the probe needles, a piece of indium was soldered onto the FTO and a piece of silver was deposited on top of the top gold contact.

The measurements were performed on a cryogenic probe station. Two probes were used, one at the silver contact and one at the indium contact. The voltage was swept over the range of -2 to 2 volts for each temperature setting. After each current measurement, the temperature was changed and the system was given time to stabilize. The ambient temperature was incremented from 80 to 370 K in steps of 10 K.



Figure 20: The probe station (left) and a close-up view of the probing needles and test sample (right).

4. Results and discussion

In the following section, I will present the results produced by simulations and experimental measurements. Together with the description of each result, I will also give a brief discussion about the outcome, and where suitable, draw conclusions. The terminology and methodology employed are described in the previous sections.

4.1 Simulation

Dark current transport mechanisms

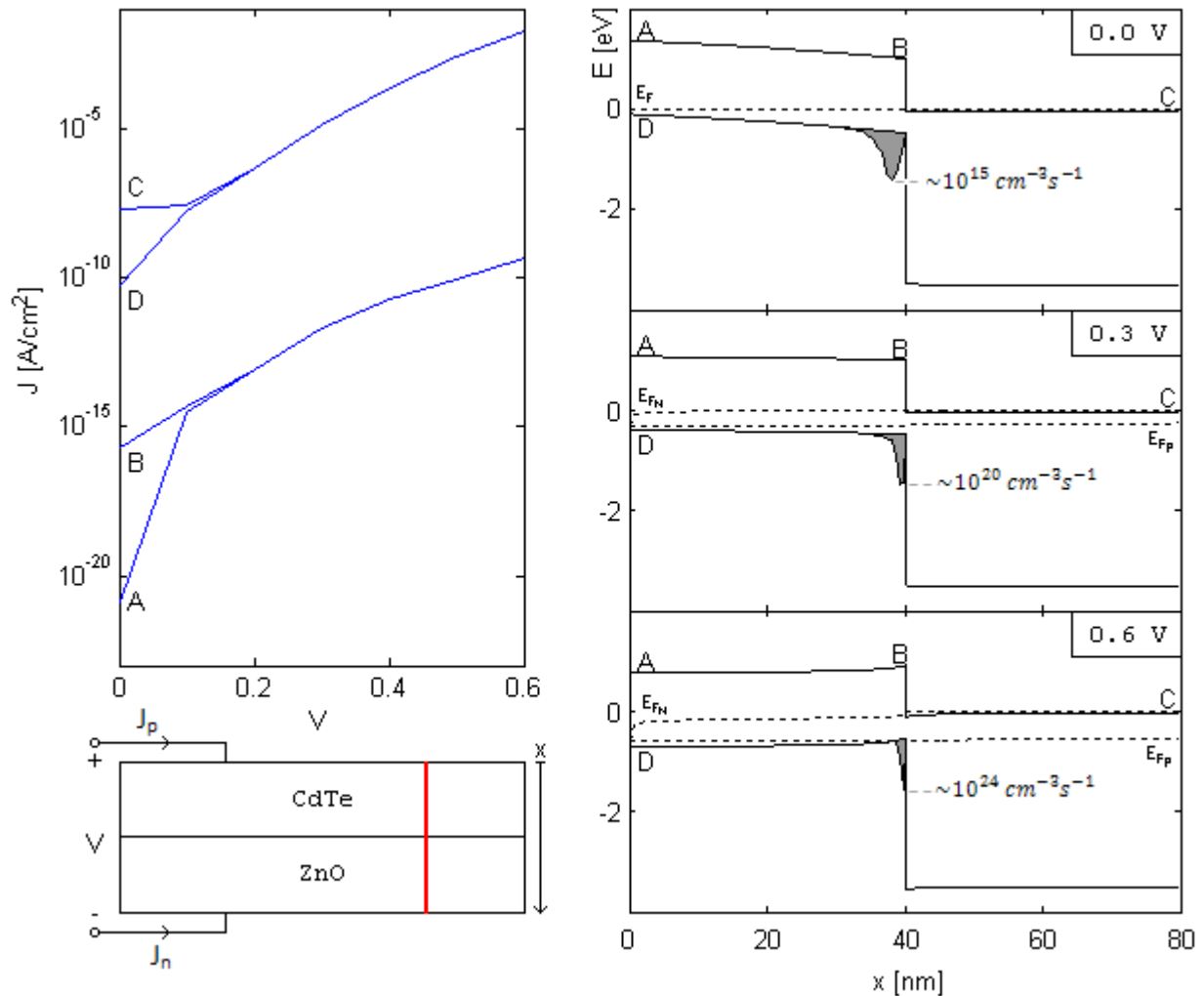


Figure 21: IV-curve (top left) for the four currents A-D in the three band diagrams (right). A is the electron current (J_n) and D is the hole current (J_p) just at the top of the CdTe layer. B is the electron current in the CdTe layer just before the ZnO layer starts, and C is the electron current at the bottom of the ZnO layer. The gray area represents the hole recombination rate as a function of x . The figure at the bottom left is a schematic representation of the structure on which the simulations were done, including voltage and current references. The red line indicates which part of the structure that the band diagrams are drawn for.

Figure 21 pictures three band diagrams for a cut line crossing the heterojunction of a simulated 2D planar CdTe/ZnO structure (bottom left in figure 21) with the same CdTe layer thickness and physical parameters as the nanowire array. The planar structure was chosen to promote a high mesh resolution while still having a reasonable computing time.

The gray shaded area is the normalized hole recombination rate as a function of x . As can be noticed, no hole recombination of significance is taking place at any other location than in the area just before the barrier, and the total rate almost (within the same order of magnitude) balances up the electron recombination rate directly after the barrier (not shown). This is explained by the way Sentaurus is modeling trap-assisted tunneling (see figure 13). If the carriers are tunneling, the electron recombination rate will differ from the hole recombination rate at the same point. As expected, the integrated total of hole recombination over the whole CdTe layer equals the hole current at D. Intrinsic and injected hole concentration in ZnO is negligible due to the large barrier, wide band gap and high level of doping ($N_D=10^{19} \text{ cm}^{-3}$).

The electron current at B is the combined current due to thermionic emission from ZnO and thermal generation from the midgap trap level in CdTe. It is five to seven orders of magnitude smaller than the hole current at D, which hints about a low rate of electrons that are thermionically transported over the barrier from the ZnO-side.

Validity of superposition principle

The difference in current through the nanowire structure under illumination and in the dark is almost constant in the low to medium-bias regime (see figure 22), thus confirming that we have a voltage-independent photocurrent which validates the superposition principle for this region. The drop in difference at higher bias could stem from the fact that the main contribution of both photocurrent and recombination current takes place in the space-charge region. This invalidates the assumption of a linear current density system, and the superposition principle can thus not be guaranteed [3].

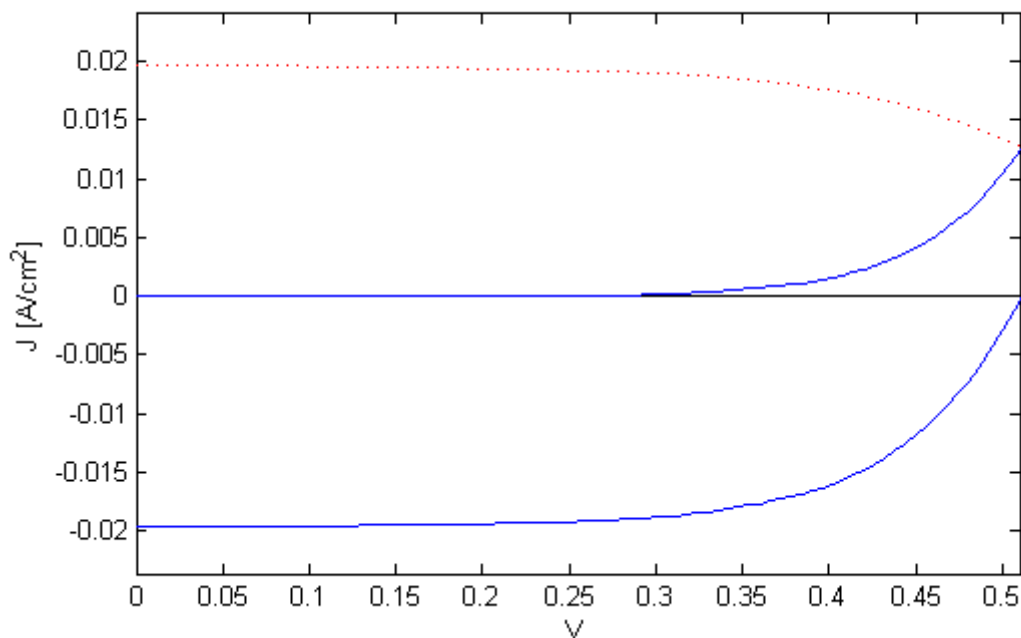


Figure 22: IV-curves for the nanowire array under illuminated (lower, blue) and dark (middle, blue) conditions. The upper, red curve is their difference.

Short-circuit current and collection efficiency

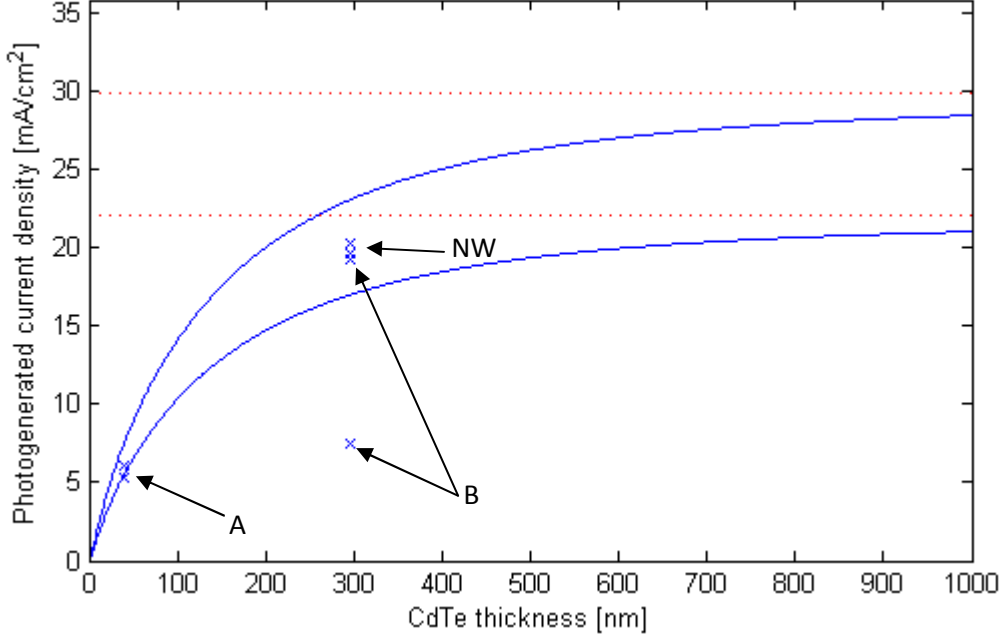


Figure 23: Theoretical dependence on CdTe layer thickness for the photogenerated current density (J_L) in planar structures, with (lower solid blue) and without (upper solid blue) reflection between the CdTe layer and air. Red dashed lines denote the maximum possible photogenerated current ($J_{L,max}$) for both cases. The blue crosses marks the photogenerated current densities (upper marker) and the short circuit current densities (lower marker) for three simulated structures: two planar cases (A, B) and the optically optimal nanowire structure (NW).

The blue curves in figure 23 are the theoretical photogenerated current density (J_L) for planar structures as a function of CdTe-layer thickness. As the thickness increases, the current density approaches its maximum ($J_{L,max}$) where all photons with energies larger than the band gap are absorbed. The upper curve represents the case where all incident photons are transmitted through the interface between air and CdTe ($T = 1$), and the lower curve is calculated with a transmission coefficient based on the refractive index n for air and CdTe through the Fresnel equation

$$T(\lambda) = 1 - \left(\frac{n_{air} - n(\lambda)}{n_{air} + n(\lambda)} \right)^2 \quad (35)$$

where $n(\lambda)$ is taken from tabulated values (see figure 35). The maximum (red dashed lines) is given by

$$J_{L,max} = \int_0^{\lambda_{Eg}} I_{AM1.5}(\lambda) \frac{q\lambda}{hc} T(\lambda) d\lambda \quad (36)$$

The blue curves are then calculated as

$$J_L(d) = J_{L,max} - \int_0^{\lambda_{Eg}} I_{AM1.5}(\lambda) \frac{q\lambda}{hc} T(\lambda) \exp(-d\alpha(\lambda)) d\lambda \quad (37)$$

where d is the thickness of the CdTe layer, α is the absorption coefficient for CdTe (tabulated, see figure 35), $I_{AM1.5}$ is the incident solar spectrum (figure 3), and λ_{Eg} is the equivalent wavelength for the bandgap of CdTe.

By putting several layers of different materials, the refractive index can be gradually changed from $n=1$ (air) to that of the absorbing material, minimizing the reflection. This has been exploited to some extent in the calculation of the generation rate matrix of our structures, because they are all modeled with a top layer of FTO which has a refraction index that is in between the refraction index of air and CdTe.

It should be noted that the solid blue lines in figure 23 represents a model where all photons that have not been absorbed at a distance d , are lost. It does not take into consideration any subsequent reflections at the underlying layers such as FTO and glass substrate. In reality, these effects would increase the photocurrent slightly.

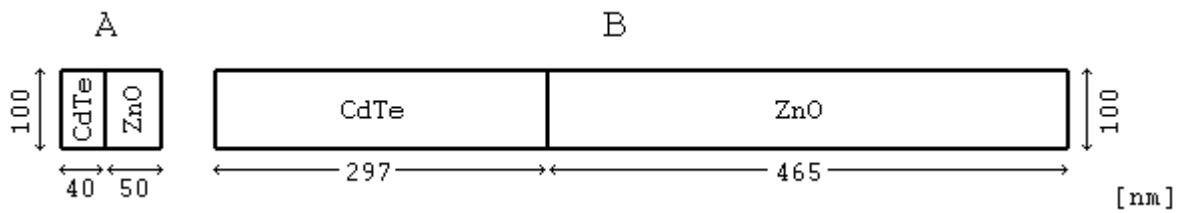


Figure 24: Diagram over the two simulated planar structures. Light is incident from the left.

The blue crosses in figure 23 marks the photogenerated current J_L and the simulated short-circuit current J_{sc} for two planar structures (A, B) and for the nanowire array (NW):

	A	B	NW
J_L [mA/cm ²]	6.07	19.30	20.28
J_{sc} [mA/cm ²]	5.33	7.55	19.67
d [nm]	40	297	297 (eff)
J_{sc}/J_L	88 %	39 %	97 %
η	1.15 %	2.10 %	6.46 %

Table 2: Photogenerated current (J_L), short-circuit current (J_{sc}), CdTe-layer thickness (d), collection efficiency (J_{sc}/J_L) and power conversion efficiency (η) for two planar devices (A, B), and the NW array.

The simulated planar structures A and B had both a top- and bottom layer of 75 nm ITO and 300 nm FTO respectively, and were placed on top of a glass substrate. Reflection at the interface between FTO and glass was properly accounted for.

The thickness of the CdTe-layer in structure B was set to correspond to the same effective thickness as the nanowire array, that is, the same volume of CdTe per area. As expected, the photogenerated current is almost as high in structure B as for the nanowire. The reason that the nanowire still has a slightly higher value could be because of its advantageous light trapping properties. What is worth to note is the difference in collection efficiency (J_{sc}/J_L) between NW and B. Obviously, since the thickness of the CdTe-layer in B is over seven times larger than that of the NW, a significant amount of electrons will recombine and never be collected (transported over to the ZnO). In structure A however, the collection efficiency is still quite high since the CdTe layer thickness is the same as the shell thickness of the NW (40 nm). On the other hand, there will not be a lot of electrons to collect, since the layer is too thin to absorb photons in the middle- to long wavelength range. The photons will reflect on the glass substrate, likely not be absorbed again, and leave the structure. In the NW

array however, the light is scattered and reflected numerous times in the structure, increasing the probability for absorption.

Surface recombination

We also wanted to investigate to which degree surface recombination had an impact on the overall efficiency of the nanowire structure. Since the nanowire geometry is cylindrical and the dimensions are small, it carries a high surface-to-volume ratio by design ($>10^5 \text{ cm}^{-1}$), and in our case the area of the surface that covers the nanowires is over eight times larger than the area they are standing on. This increases the likelihood that a minority carrier scatters to the surface, where also most high-energy photons with short wavelengths are absorbed. Since we then have a high minority carrier concentration close to the surface, any recombination in this area will have a big impact on the short-circuit current and efficiency of the cell. Since a large surface coverage at the same time is beneficial, due to the aforementioned separation of optical absorptance depth and minority carrier diffusion length, efforts to reduce the surface recombination velocity (the speed at which minority carriers diffuse towards the surface due to a lower concentration gradient caused by the recombination) is of importance. A type of recombination that is characteristic to surfaces is recombination through interruptions of the periodicity in the crystal lattice, *dangling bonds*. Reduction of dangling bonds is called *surface passivation*, where an additional insulating layer is placed on top on the absorbing material.

In Sentaurus, surface recombination is specified as a velocity at the interface between two sections. In order to analyze the impact of surface recombination in the model, we added an outer layer of vacuum, and gradually increased the recombination velocity at the interface between CdTe and this pseudo-material. Interestingly, no effect on the current-voltage characteristics could be found, even at very high velocities of 10^8 cm/s . By analysis of the simulation results, it was confirmed that Sentaurus does take the surface recombination velocity into account, but that it had no discernible influence on the electron concentration at the surface.

Minority carrier lifetime in CdTe

The minority carrier lifetime for CdTe in the NW almost exclusively had an impact on the open-circuit voltage (figure 25). When the lifetime increases, a higher amount of generated carriers in the CdTe survives from recombination and will be collected by the junction. The current of collected carriers increases, thus balancing the opposing dark current (which scales exponentially with applied bias) at a higher bias for longer lifetimes. The values at the upper x-axis in figure 25 reflect the corresponding diffusion length for each lifetime, based on the electron mobility in table 1 and equation 33.

In figure 26, we see the IV-curves for the two planar structures A and B. Structure A, with a CdTe thickness of 40 nm, demonstrates the same characteristics as the NW regarding the short-circuit current. In B however, there is a slight increase in J_{sc} for longer lifetimes.

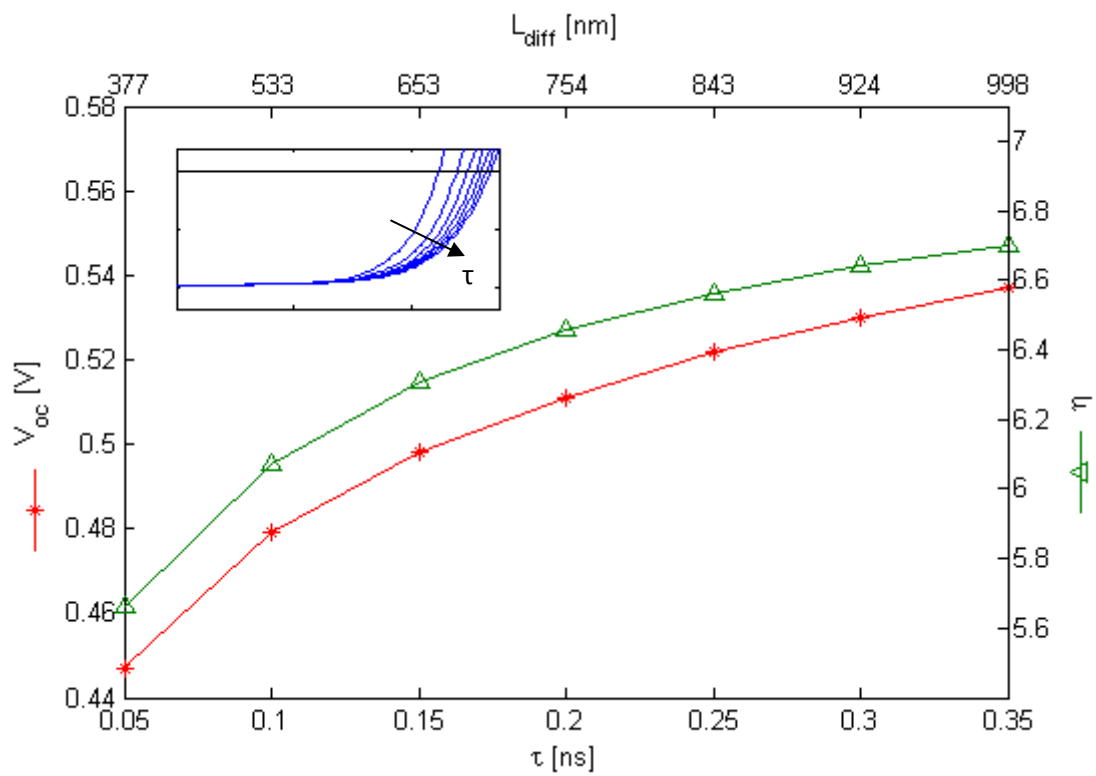


Figure 25: Impact of the minority carrier lifetime in CdTe for the NW. The inset shows the corresponding IV-curves, with a J_{sc} of 19.67 mA/cm^2 .

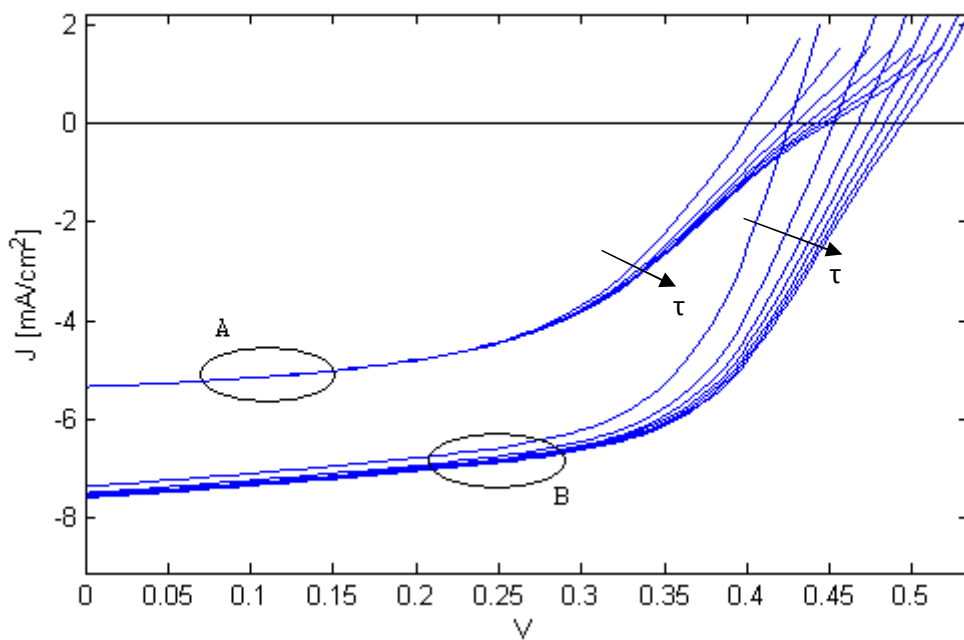


Figure 26: IV curves for the two planar structures, with CdTe minority carrier lifetimes increasing from 0.05 to 0.35 ns, in steps of 0.05 ns.

Doping in ZnO

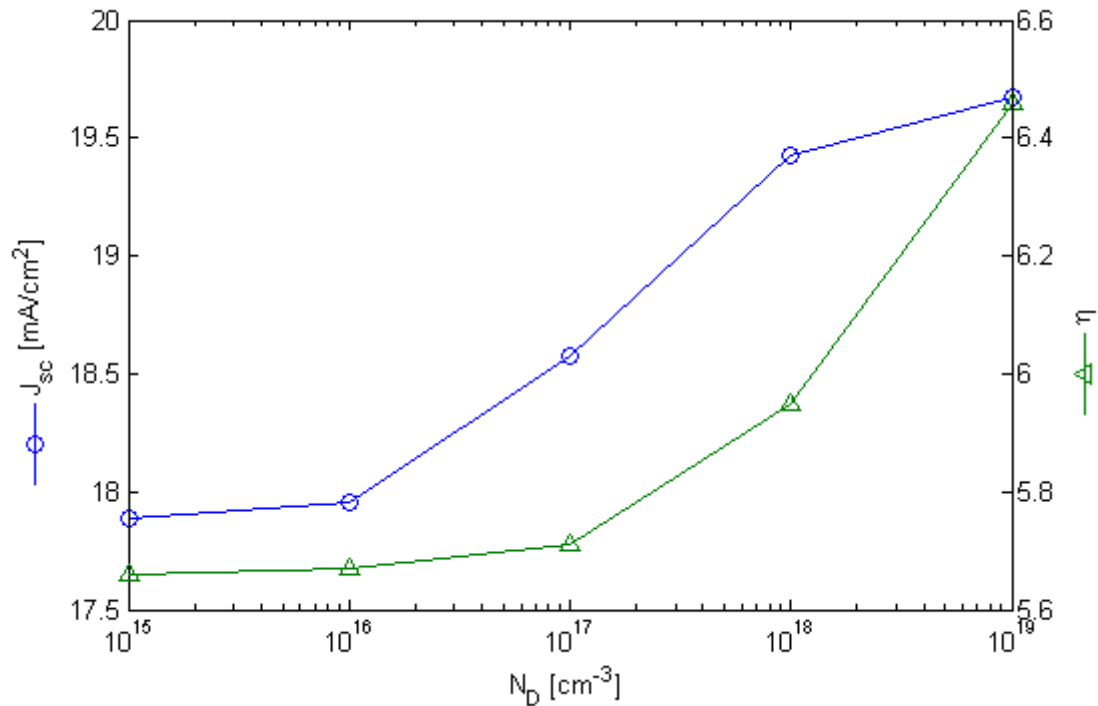


Figure 27: Impact of ZnO core n-doping concentration (N_D) on the short-circuit current (J_{sc}) and power conversion efficiency (η). The CdTe shell has a fixed p-doping of 10^{17} cm^{-3} .

In figure 27 we see how the amount of n-doping of the ZnO core affects the short-circuit current and power conversion efficiency. Since a higher amount of n-doping results in a greater band bending at the CdTe-side, this will improve the collection efficiency because the wider space charge region swiftly pulls the generated charge carriers apart. This is illustrated in figure 28. Very high doping concentrations could be detrimental, since the mobility degrades due to increased scattering with the impurity atoms [11]. It should be noted that the physical model we used does not take into account any doping dependence of the mobility. Any recombination through defect levels is highly unlikely at room temperature since the band gap of ZnO is large (see figure 8). The p-doping concentration of CdTe was fixed at 10^{17} cm^{-3} which is low enough for minimal electron recombination rate (see eq. 34), while at the same time being sufficient for good hole conductivity.

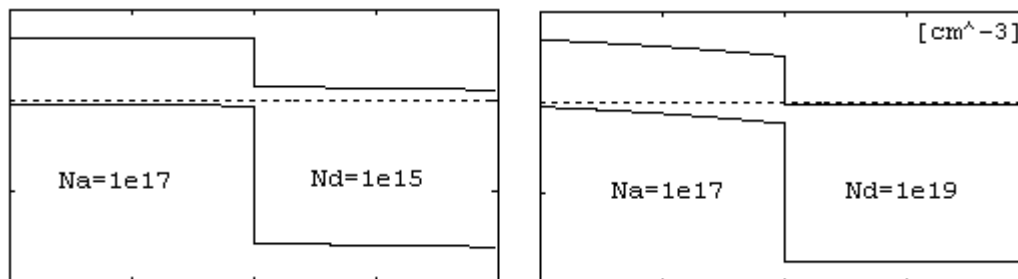


Figure 28: Band diagram for the heterojunction, with different n-doping concentrations in the ZnO-core.

Impact of TAT

The TAT process was shown to have a major impact on the overall charge carrier transport characteristics, as can be observed in figure 29. It reveals the importance of accurately taking into account the defect levels and their concentrations in the vicinity of the ZnO/CdTe heterojunction. As suggested by [6][9], defect states in the CdTe allows for majority charge carrier exchange between the semiconductors through a tunneling-recombination step process (see figure 13), effectively increasing the dark current. In the TAT model we implemented, we simply defined the defect level to be in the middle of the bandgap. Neither is any defect concentration specified, since Sentaurus models TAT with a dependence on minority carrier lifetime which already is supposed to take defect density into account. Nevertheless, the results give a qualitative understanding of the influence of tunneling to and from defect states close to the CdTe/ZnO interface.

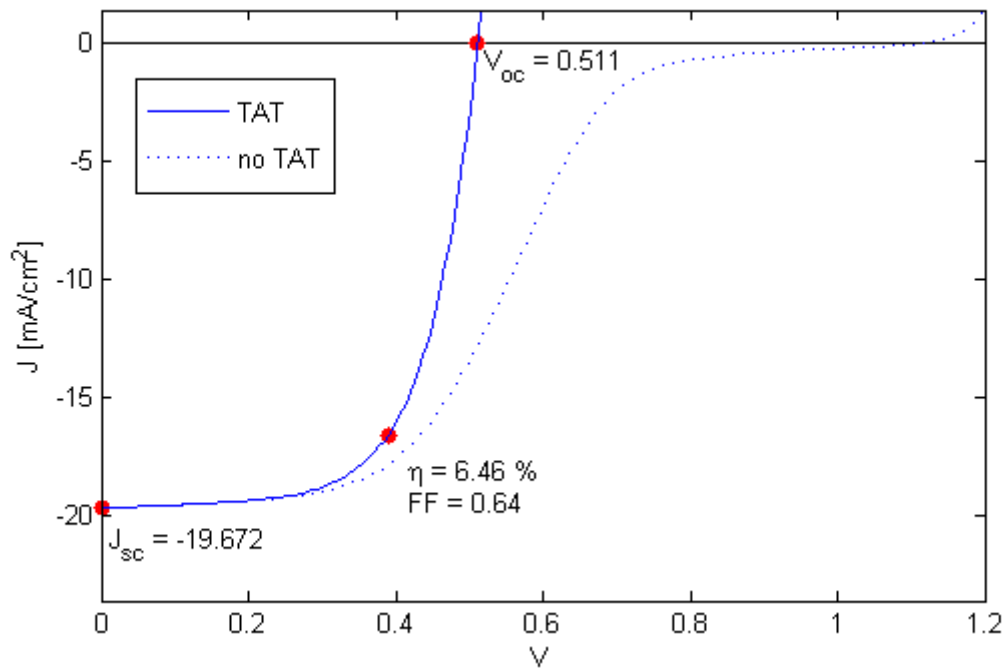


Figure 29: IV curve for the NW structure under illumination, simulated with (solid blue) and without (dotted blue) Trap-Assisted Tunneling.

Temperature dependence

Dark current simulation results for the nanowire were produced for temperatures between 50 and 350 K. The current exhibits a polynomial dependence on temperature (see figure 31, left), which partially can be attributed to increased diffusivity for higher temperatures. This implies that diffusion in the bulk regions is the limiting factor for the dark current in the model. The current increases exponentially with applied bias as expected (see figure 31, right).

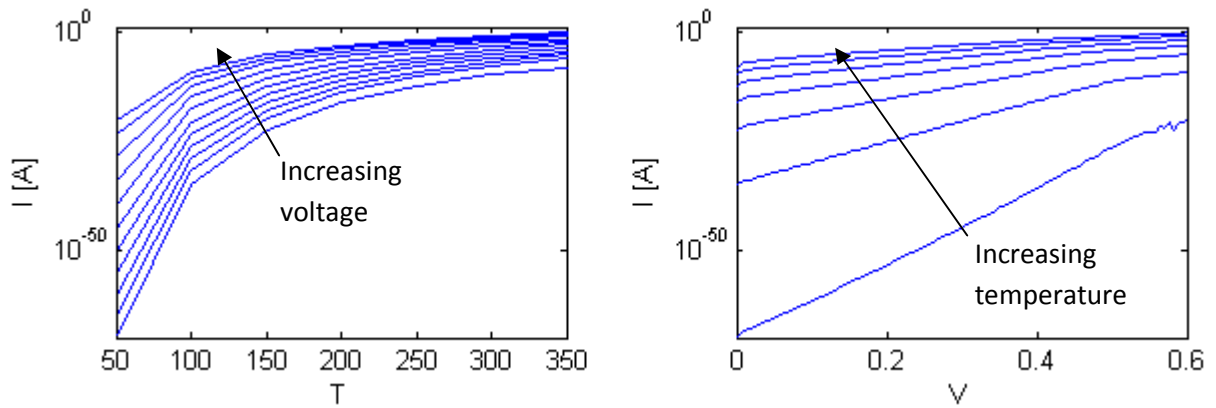


Figure 31: Dark current temperature dependence for the simulated nanowire array. The voltage is increased from 0 to 0.6 V in steps of 0.06 V, and the temperature is increased from 50 to 350 K in steps of 50 K.

4.2 Measurements

Figure 32 shows the IV-curves for the experimentally measured data.

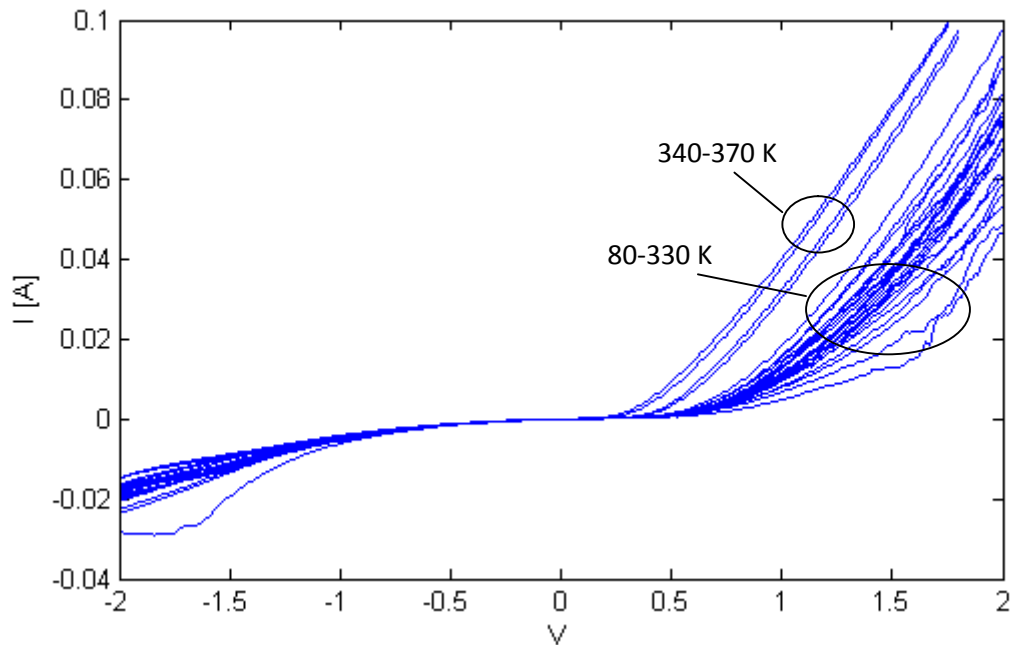


Figure 32: Measured dark current, linear plot.

Figure 33 is the corresponding I-T plot with applied bias as a parameter. The dark current density for the planar structure was almost totally independent on temperature, except for a small but significant increase at temperatures above 350 K.

This is not in agreement with our simulated results (see figure 31). The difference could originate from several reasons. One being the fact that no shunt leakage path is taken into account in the simulation. Another reason could be non-Ohmic contact behavior between the gold layer and CdTe. The inconclusive results underline the importance of continuous verification and validation of simulation models and experimental prototypes. In our case, this mainly points to the direction of further refinement of the sample quality and production methods, since the current is expected to have an exponential dependence on temperature [9].

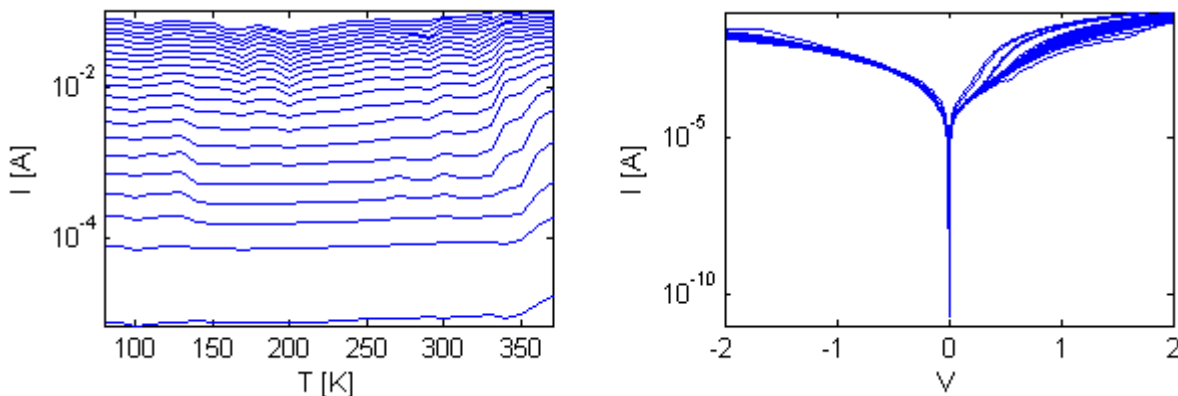


Figure 33: Measured current vs. temperature. The left diagram shows the current as a function of temperature, with applied voltage (increasing from 0.01 to 2 V, in steps of 0.1 V) as a parameter. The right diagram shows the current as a function of applied bias, with temperature (increasing from 80 to 370 K, in steps of 10 K) as a parameter.

Fit to single diode circuit model

The measured data was fitted to a single diode circuit model, having the current-voltage relationship:

$$I = I_0 \left(e^{\frac{V - IR_s}{nk_B T}} - 1 \right) + \frac{(V - IR_s)}{R_{sh}} \quad (38)$$

where n is the diode *ideality factor*. The aim of this was to deduce physical properties of the test sample from the extracted parameters. The results can be seen in figure 34. The series resistance R_s is in the region of 10 Ohm for all temperatures. The shunt resistance R_{sh} proved to be impossible to extract, it had a very large spread. This is because a big difference in shunt resistance can be compensated by a very small change in the diode saturation current I_0 . The diode ideality factor is decreasing from 34 (which is very high) to 3. The diode saturation current is around 0.1 mA.

No physical parameters could be extracted, since the data does not show any clear trend. There might be other current rectifying processes in the device that are not represented by the single diode model. Also, the measurements were disturbed and contained errors at some temperatures (see figure 32).

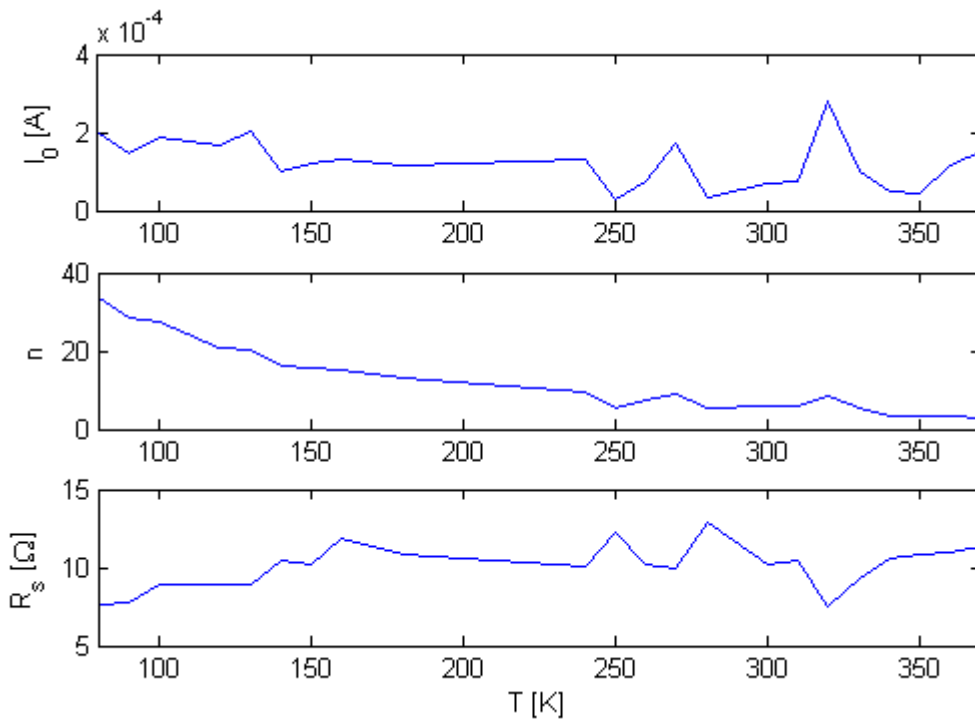


Figure 34: Extracted parameters for experimental data, when fitted to the single diode circuit model.

5. Conclusions

- Main dark current mechanism is likely tunneling and recombination through defects, and incorporating this process in the model is important.
- The superposition principle is valid in the low- to medium-bias regime.
- The vertical core/shell nanowire array setup warrants good absorption and collection efficiency compared with conventional planar structures.
- The open-circuit voltage increases with longer electron lifetime in CdTe.
- Increasing n-doping in ZnO results in an increased short-circuit current.
- Fitting of IV-curves can give a quick glimpse into the overall behavior of the device, but is not valuable for extraction of several physical parameters at once. This requires additional measurement techniques.

Future work

As has been pointed out in the previous section, further investigations should be made concerning mainly two areas. Firstly, since this project is based around the description and optimization of electrical transport in a structure with pre-determined dimensions for maximum light absorption, no information is given whether this is the best combination overall. There might be other combinations of length, diameter, periodicity and shell thickness that due to better carrier collection have higher power conversion efficiency than the structure with the best absorption.

Secondly, a more thorough experimental verification of the model needs to be done by the production of a real solar cell device. Measurements of physical properties should be made, such as electron lifetime in CdTe, charge carrier mobilities, and surface recombination velocity. Trap densities and their ionization energies should also be investigated, with particular focus around the heterojunction interface.

6. Bibliography

- [1] Shockley, W., & Queisser, H. J. (1961). Detailed Balance Limit of Efficiency of p-n Junction Solar Cells. *Journal of Applied Physics* , 32 (3), 510-519. DOI: 10.1063/1.1736034
- [2] Honsberg, C., & Bowden, S., *PV Education*, <http://www.pveducation.org/>
- [3] Lindholm, F. A., Fossum, J. G., Burgess, E. L. (1979). Application of the superposition principle to solar-cell analysis. *IEEE Transactions on Electron Devices*, 165 - 171. DOI: 10.1109/T-ED.1979.19400
- [4] Erik C. Garnett, M. L. (2011). Nanowire Solar Cells. *Annual Review of Materials Research* . , 41. DOI: 10.1146/annurev-matsci-062910-100434
- [5] Kayes, B. M., Atwater, H. A., & Lewis, N. S. (2005). Comparison of the device physics principles of planar and radial p-n junction nanorod solar cells. *Journal of Applied Physics* , 97 (11). DOI: 10.1063/1.1901835
- [6] Aranovich, J. A., Golmayo, D., Fahrenbruch, A. L., & Bube, R. H. (1980). Photovoltaic properties of ZnO/CdTe heterojunctions prepared by spray pyrolysis. *Journal of Applied Physics* , 4260 - 4268. DOI: 10.1063/1.328243
- [7] Consonni, V., Rey, G., Bonaimé, J., Karst, N., Doisneau, B., Roussel, H., et al. (2011). Synthesis and physical properties of ZnO/CdTe core shell nanowires grown by low-cost deposition methods. *Applied Physics Letters* , 98 (11). DOI: 10.1063/1.3567764
- [8] Fan, Z., & Lu, J.G. (2005). Zinc Oxide Nanostructures: Synthesis and Properties. *Journal of Nanoscience and Nanotechnology* , 5 (10), 1561-1573. DOI: 10.1166/jnn.2005.182
- [9] Mancini, A. M., Pierini, P., Valentini, A., & Vasanelli, L. (1984). ZnO/CdTe heterojunctions prepared by r.f. sputtering. *Thin Solid Films* , 124 (1), 85-92. DOI: 10.1016/0040-6090(85)90032-X
- [10] Michallon, J., Zanucoli, M., Kaminski-Cachopo, A., Consonni, V., Morand, A., Bucci, D., et al. (2012). Comparison of optical properties of Si and ZnO/CdTe core/shell nanowire arrays. *Materials Science and Engineering: B* , 665–669. DOI: 10.1016/j.mseb.2012.10.037
- [11] Sze, S., & Lee, M. (2012). *Semiconductor Devices - Physics and Technology*. Wiley.
- [12] *Sentaurus Device User Guide*, Synopsys Inc., 2011
- [13] Horio, K., & Yanai, H. (1990). Numerical modeling of heterojunctions including the thermionic emission mechanism at the heterojunction interface. *IEEE Transactions on Electron Devices* , 1093 - 1098. DOI: 10.1109/16.52447
- [14] Hurkx, G., Klaassen, D., & Knuyvers, M. (1992). A new recombination model for device simulation including tunneling. *IEEE Transactions on Electron Devices* , 331 - 338. DOI: 10.1109/16.121690
- [15] Wolpert, D., & Ampadu, P. (2012). *Managing Temperature Effects in Nanoscale Adaptive Systems*. Springer. DOI: 10.1007/978-1-4614-0748-5_2

7. Appendix

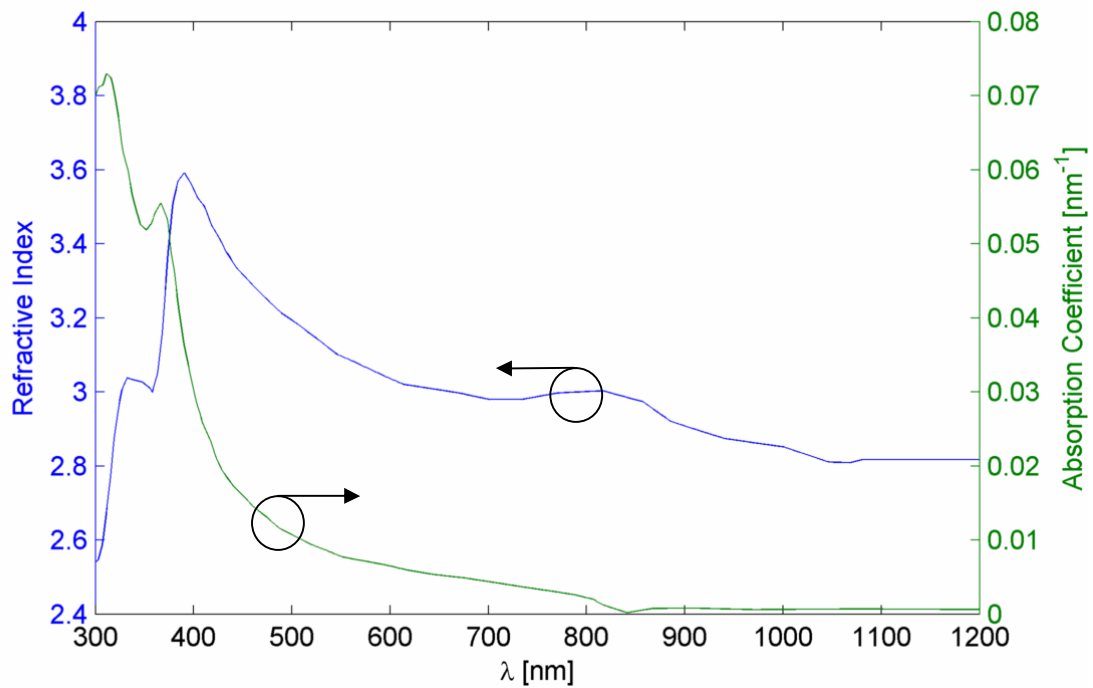


Figure 35: Refractive index and absorption coefficient for CdTe.

8. List of abbreviations

AFMM	Aperiodic Fourier Modal Method
CdTe	Cadmium Telluride
FF	Fill Factor
FTO	Fluorine doped Tin Oxide
NW	Nanowire
RCWA	Rigorous Coupled Wave Analysis
SRH	Shockley-Read-Hall
TAT	Trap-Assisted Tunneling
TCAD	Technology Computer Aided Design
ZnO	Zinc Oxide